



**Defense Threat Reduction Agency**  
8725 John J. Kingman Road, MS  
6201 Fort Belvoir, VA 22060-6201



**DTRA-TR-12-70**

# TECHNICAL REPORT

---

## Single-Crystal Bismuth Iodine Gamma-Ray Spectrometers

Approved for public release, distribution is unlimited.

February 2013

HDTRA1-07-1-0013

James E. Baciak et al.

Prepared by:  
University of Florida  
Dept. of Nuclear and  
Radiological Engineering  
202 NSC  
Gainesville, FL 32611

**DESTRUCTION NOTICE:**

Destroy this report when it is no longer needed.  
Do not return to sender.

PLEASE NOTIFY THE DEFENSE THREAT REDUCTION  
AGENCY, ATTN: DTRIAC/ J-3 ONIUI , 8725 JOHN J. KINGMAN ROAD,  
MS-6201, FT BELVOIR, VA 22060-6201, IF YOUR ADDRESS  
IS INCORRECT, IF YOU WISH THAT IT BE DELETED FROM THE  
DISTRIBUTION LIST, OR IF THE ADDRESSEE IS NO  
LONGER EMPLOYED BY YOUR ORGANIZATION.

# REPORT DOCUMENTATION PAGE

*Form Approved  
OMB No. 0704-0188*

Public reporting burden for this collection of information is estimated to average 1 hour per response, including the time for reviewing instructions, searching existing data sources, gathering and maintaining the data needed, and completing and reviewing this collection of information. Send comments regarding this burden estimate or any other aspect of this collection of information, including suggestions for reducing this burden to Department of Defense, Washington Headquarters Services, Directorate for Information Operations and Reports (0704-0188), 1215 Jefferson Davis Highway, Suite 1204, Arlington, VA 22202-4302. Respondents should be aware that notwithstanding any other provision of law, no person shall be subject to any penalty for failing to comply with a collection of information if it does not display a currently valid OMB control number. **PLEASE DO NOT RETURN YOUR FORM TO THE ABOVE ADDRESS.**

<b>1. REPORT DATE (DD-MM-YYYY)</b> 00-02-2013		<b>2. REPORT TYPE</b> Technical		<b>3. DATES COVERED (From - To)</b>	
<b>4. TITLE AND SUBTITLE</b>  Single-Crystal Bismuth Iodide Gamma-Ray Spectrometers		<b>5a. CONTRACT NUMBER</b>			
		<b>5b. GRANT NUMBER</b> HDTRA1-07-1-0013			
		<b>5c. PROGRAM ELEMENT NUMBER</b>			
<b>6. AUTHOR(S)</b>  James E. Baciak, Juan C. Nino, Wei Qiu, and Azaree Lintereur		<b>5d. PROJECT NUMBER</b>			
		<b>5e. TASK NUMBER</b>			
		<b>5f. WORK UNIT NUMBER</b>			
<b>7. PERFORMING ORGANIZATION NAME(S) AND ADDRESS(ES)</b>  University of Florida Dept. of Nuclear and Radiological Engineering 202 NSC Gainesville, FL 32611		<b>8. PERFORMING ORGANIZATION REPORT NUMBER</b>			
<b>9. SPONSORING / MONITORING AGENCY NAME(S) AND ADDRESS(ES)</b>  Defense Threat Reduction Agency 8725 John J. Kingman Road STOP 6201 Fort Belvoir, VA 22060 PM/D. Petersen		<b>10. SPONSOR/MONITOR'S ACRONYM(S)</b> DTRA			
		<b>11. SPONSOR/MONITOR'S REPORT NUMBER(S)</b> DTRA-TR-12-70			
<b>12. DISTRIBUTION / AVAILABILITY STATEMENT</b>  Approved for public release, distribution is unlimited.					
<b>13. SUPPLEMENTARY NOTES</b>					
<b>14. ABSTRACT</b>  The main objective of this 3-year project is to grow high quality BiI <sub>3</sub> single crystals (>1cm <sup>3</sup> in volume) via a high temperature modified Bridgman crystal growth technique. We will then test and analyze the crystals using a variety of techniques to determine crystal quality (lattice parameters, lattice strain, impurities, etc.) and potential methods to improve BiI <sub>3</sub> crystals. Finally, test structures will be designed and their performance will be assessed using a variety of small, calibrated gamma-ray sources available at the University of Florida.					
<b>15. SUBJECT TERMS</b>  Bridgman Crystals PVT Lattice strain					
<b>16. SECURITY CLASSIFICATION OF:</b>			<b>17. LIMITATION OF ABSTRACT</b>  SAR	<b>18. NUMBER OF PAGES</b>  60	<b>19a. NAME OF RESPONSIBLE PERSON</b> David Petersen
<b>a. REPORT</b> Unclassified	<b>b. ABSTRACT</b> Unclassified	<b>c. THIS PAGE</b> Unclassified			<b>19b. TELEPHONE NUMBER (include area code)</b> (703) 767-3164

## CONVERSION TABLE

Conversion Factors for U.S. Customary to metric (SI) units of measurement.

MULTIPLY → BY ← DIVIDE  
TO GET ← BY → TO GET

angstrom	1.000 000 x E -10	meters (m)
atmosphere (normal)	1.013 25 x E +2	kilo pascal (kPa)
bar	1.000 000 x E +2	kilo pascal (kPa)
barn	1.000 000 x E -28	meter <sup>2</sup> (m <sup>2</sup> )
British thermal unit (thermochemical)	1.054 350 x E +3	joule (J)
calorie (thermochemical)	4.184 000	joule (J)
cal (thermochemical/cm <sup>2</sup> )	4.184 000 x E -2	mega joule/m <sup>2</sup> (MJ/m <sup>2</sup> )
curie	3.700 000 x E +1	*giga bacquerel (GBq)
degree (angle)	1.745 329 x E -2	radian (rad)
degree Fahrenheit	t <sub>k</sub> = (t°f + 459.67)/1.8	degree kelvin (K)
electron volt	1.602 19 x E -19	joule (J)
erg	1.000 000 x E -7	joule (J)
erg/second	1.000 000 x E -7	watt (W)
foot	3.048 000 x E -1	meter (m)
foot-pound-force	1.355 818	joule (J)
gallon (U.S. liquid)	3.785 412 x E -3	meter <sup>3</sup> (m <sup>3</sup> )
inch	2.540 000 x E -2	meter (m)
jerk	1.000 000 x E +9	joule (J)
joule/kilogram (J/kg) radiation dose absorbed	1.000 000	Gray (Gy)
kilotons	4.183	terajoules
kip (1000 lbf)	4.448 222 x E +3	newton (N)
kip/inch <sup>2</sup> (ksi)	6.894 757 x E +3	kilo pascal (kPa)
ktap	1.000 000 x E +2	newton-second/m <sup>2</sup> (N-s/m <sup>2</sup> )
micron	1.000 000 x E -6	meter (m)
mil	2.540 000 x E -5	meter (m)
mile (international)	1.609 344 x E +3	meter (m)
ounce	2.834 952 x E -2	kilogram (kg)
pound-force (lbs avoirdupois)	4.448 222	newton (N)
pound-force inch	1.129 848 x E -1	newton-meter (N-m)
pound-force/inch	1.751 268 x E +2	newton/meter (N/m)
pound-force/foot <sup>2</sup>	4.788 026 x E -2	kilo pascal (kPa)
pound-force/inch <sup>2</sup> (psi)	6.894 757	kilo pascal (kPa)
pound-mass (lbf avoirdupois)	4.535 924 x E -1	kilogram (kg)
pound-mass-foot <sup>2</sup> (moment of inertia)	4.214 011 x E -2	kilogram-meter <sup>2</sup> (kg-m <sup>2</sup> )
pound-mass/foot <sup>3</sup>	1.601 846 x E +1	kilogram-meter <sup>3</sup> (kg/m <sup>3</sup> )
rad (radiation dose absorbed)	1.000 000 x E -2	**Gray (Gy)
roentgen	2.579 760 x E -4	coulomb/kilogram (C/kg)
shake	1.000 000 x E -8	second (s)
slug	1.459 390 x E +1	kilogram (kg)
torr (mm Hg, 0° C)	1.333 22 x E -1	kilo pascal (kPa)

\*The bacquerel (Bq) is the SI unit of radioactivity; 1 Bq = 1 event/s.

\*\*The Gray (GY) is the SI unit of absorbed radiation.

## **Objectives**

The main objective of this 3-year project is to grow high quality  $\text{BiI}_3$  single crystals ( $> 1 \text{ cm}^3$  in volume) via a high temperature modified Bridgman crystal growth technique. We will then test and analyze the crystals using a variety of techniques to determine crystal quality (lattice parameters, lattice strain, impurities, etc.) and potential methods to improve  $\text{BiI}_3$  crystals. Finally, test structures will be designed and their performance will be assessed using a variety of small, calibrated gamma-ray sources available at the University of Florida. We will measure radiation sensitivity, charge carrier mobility and lifetimes, and noise characteristics of the test structures (basic material properties for  $\text{BiI}_3$ ). While the main objectives of the project have not changed, more emphasis is being placed on  $\text{BiI}_3$  crystal growth principles and materials analyses. This increase in materials properties assessment is based on suggestions from the DTRA review team during the kickoff meeting in May 2007.

### **1.0 Crystal Growth Techniques of $\text{BiI}_3$**

While the PVT method can produce high quality but small volume crystals, the vertical Bridgman technique can grow crystals with larger volume but the crystal quality is not as good as those grown from PVT.<sup>1-4</sup> We primarily discuss the growth of  $\text{BiI}_3$  single crystals using the modified vertical Bridgman (MVB) technique. The quality of the crystals grown under different conditions was evaluated and compared to that of crystals grown by PVT method.

#### **1.1 Vertical Bridgman Technique**

As the name says, this technique is named after P. W. Bridgman who is the first one using this method to grow a series of metal single crystals.<sup>5</sup> The principle of this technique involves lowering a crucible through a furnace so that the freezing starts at the lowest point in the crucible and the solidification interface slowly moves up along the crucible. The movement rates for such processes range from around 0.1 to 200 mm/h.<sup>6</sup> A typical vertical Bridgman system is shown in Figure 1. The movement of the crucible is controlled by a dropping motor. A longitudinal temperature profile is established at the center of the furnace with specific temperature gradient near the melting point of the material. The hole in the lid should be small and the lid should fit well with the furnace body to prevent thermal disturbance.

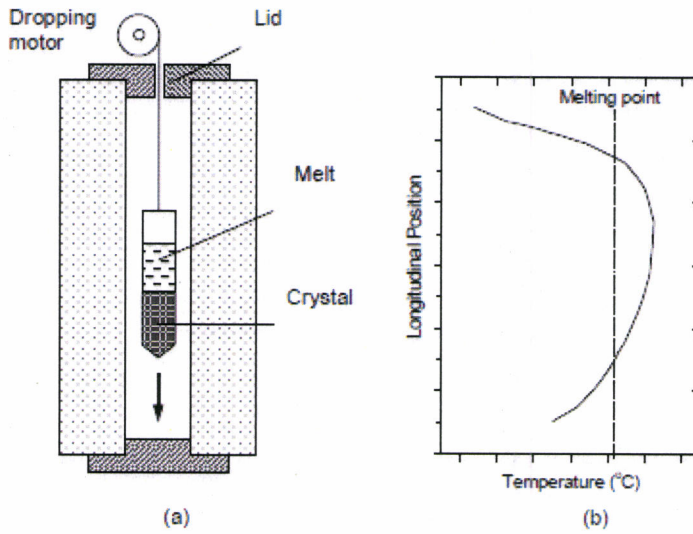


Figure 1. A typical Bridgman growth furnace setup. (a) Schematic diagram for the furnace. (b) Longitudinal temperature profile of the furnace.

The crystal growth with vertical Bridgman method can use a seed or no seed. A non-seeded Bridgman method relies on random nucleation to produce a single crystal which then propagates to form one large crystal through the whole frozen charge. The formation of just one nucleus requires a small nucleation volume. Thus the crucibles are normally shaped with sharp tips to meet the nucleation criteria, as illustrated in Figure 3-1(a). For a seeded Bridgman growth, the crucible shape is not that important. Normally a flattened bottom is made to accommodate the seed material. The most obvious requirement for a crucible is that it should not react with the crystals within the temperature range of crystal growth. It also should have a smaller coefficient of thermal expansion than the crystal to avoid the induced strain and stress during cooling.

For vertical Bridgman crystal growth, the quality of the single crystal is largely determined by the control of heat flow during crystallization. The thermal conditions of a practical crystal growth system are rather complicated, thus analytical solutions are not possible without simplifications and assumptions.<sup>7</sup> In the following discussion, it is assumed that the melt is a single component material, the density of the melt and its crystal are the same, temperature gradients within the crystal transverse to the growth direction are negligible, and the solid-liquid interface is planar. During crystal growth, a heat balance is set up by the conservation of heat flux at the interface, which can be written as<sup>8</sup>

$$\rho_s L R = K_s G_s - K_L G_L \quad (1)$$

where  $K_s$  and  $K_L$  are the thermal conductivity of solid and liquid ( $\text{cal}/(\text{cm}\cdot{}^\circ\text{C}\cdot\text{s})$ ),  $G_s$  and  $G_L$  are the temperature gradient in solid and liquid at the solid-liquid interface ( ${}^\circ\text{C}/\text{cm}$ ),

$\rho_s$  is the density of solid ( $\text{g}/\text{cm}^3$ ),  $L$  is the latent heat of melt ( $\text{cal/g}$ ), and  $R$  is the growth rate ( $\text{cm/s}$ ). The left side in Equation (1) indicates the heat generated at the interface due to solidification. The first term on the right side is the heat flux going out of the solid-liquid interface. The second term on the right side refers to the heat flux coming into the solid-liquid interface. Equation (1) indicates that the growth rate  $R$  can be controlled by independently adjusting  $G_s$  and  $G_L$ . This is important as growing good single crystals requires that the temperature gradient be high and the growth rate remain low. The temperature gradient in liquid ( $G_L$ ) is directly proportional to the heat flux in the liquid at the solid-liquid interface. The temperature gradient in solid ( $G_s$ ) is normally determined empirically or through heat flow calculations. In a cylindrical system, the heat conduction in solid can be described as<sup>6</sup>

$$\frac{\partial}{\partial z} \left[ K_s \frac{\partial T}{\partial z} \right] = \rho_s c_s \left[ \frac{\partial T}{\partial z} + R \frac{\partial T}{\partial z} \right] \quad (2)$$

where  $c_s$  is the specific heat of solid ( $\text{cal}/(\text{g}\cdot^\circ\text{C})$ ), and  $z$  is the coordinate parallel to the growth direction. Physically, the term on the left represents the net rate of heat conduction away from the solid per unit volume. The first term on the right side represents the decrease rate of internal energy per unit volume. The second term on the right side is the rate of energy released per unit volume due to interface moving. Some simplifications need to be made to solve equation (2). For example, in the case of floating zone (crucibleless) growth, assuming the crystal has a cylindrical shape, temperature gradients along the transverse direction are negligible, and heat transfer from the crystal to surrounding is by convection. At steady state, the temperature gradient in solid at the solid-liquid interface is given by<sup>8</sup>

$$G_s = (T_m - T_0) \sqrt{\left( \frac{R}{2\alpha_s} \right)^2 + \frac{2h}{rK_s}} - \frac{R}{2\alpha_s} \quad (3)$$

where  $T_0$  is the ambient temperature ( $^\circ\text{C}$ ),  $T_m$  is the melting point of the crystal,  $\alpha_s$  is the thermal diffusivity of the solid crystal ( $K_s/\rho_s c_s$ ,  $\text{cm}^2/\text{s}$ ),  $h$  is the heat transfer coefficient from solid to ambient ( $\text{cal}/(\text{cm}^2\cdot^\circ\text{C}\cdot\text{s})$ ), and  $r$  is the radius of crystal (cm). Since the growth rate  $R$  is usually small, when  $R/2\alpha_s \ll 1$ , equation (3) becomes

$$G_s \approx (T_m - T_0) \sqrt{\frac{2h}{rK_s}}. \quad (4)$$

For crystals with high melting point,  $(T_m - T_0)$  is large and the heat transfer coefficient  $h$  is increased by radiation heat transfer. The attainable  $G_s$  can be as high as  $100^\circ\text{C}/\text{cm}$  or more. For low melting point crystals, external cooling has to be applied to achieve steep gradients.

It should be noted that the analytical solutions cannot completely explain and predict the crystal growth in a practical vertical Bridgman system. This is mainly because the simplifying assumptions usually tend to discard some important details which control crystal growth.<sup>9-10</sup> Accordingly, numerical studies have been performed to gain more understandings in the vertical Bridgman growth process.<sup>7,11-18</sup> Studies have been focused on controlling the solid-melt interface shape,<sup>11,13</sup> models of the heat and mass transfer,<sup>14,15,18</sup> and the influence of the thermal environment and process parameters.<sup>16-17</sup> Accurate material thermal properties and operating environment are required for successful numerical predictions.

## 1.2 Physical Vapor Transportation Technique

The crystal growth by the PVT method is typically conducted in closed or semi-closed systems. If the vapor pressure of a material at a desired growth temperature exceeds  $10^{-2}$  torr, it may be efficiently grown by the PVT method.<sup>19</sup> In the PVT process, an ampoule containing a polycrystalline source of the desired material is heated to a temperature at which the material starts to sublime at a rate leading to crystal growth. The ampoule is typically placed in a furnace that provides a temperature gradient over the length of the ampoule, so that the polycrystalline source material sublimes at the higher temperature and deposits at the end of the ampoule where the temperature is lower. This temperature difference causes the different vapor pressure at two ends of the ampoule and forces the material transport from the source to the cooler end. The PVT system can adopt horizontal or vertical set up. A typical horizontal PVT system is illustrated in Figure 2.

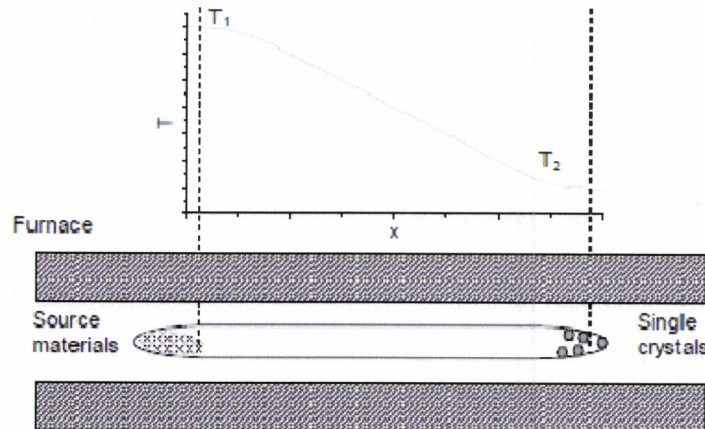


Figure 2. Schematic diagram of physical vapor transport system.<sup>20</sup>

For crystal growth by PVT method, the growth temperature  $T_2$  should exceed about one-third of the melting temperature of the crystal.<sup>6</sup> The temperature  $T_1$  is fixed so that the crystal grows at an acceptable rate which can be deduced from simple theory as follow. The vapor pressure can be expressed in the form of

$$P = P_0 e^{-\Delta H_s / RT} \quad (5)$$

then the rate of deposition in an ideal case with an evacuated ampoule is<sup>6</sup>

$$f = P_0 \left[ e^{-\Delta H_{s1} / RT_1} - e^{-\Delta H_{s2} / RT_2} \right] \sqrt{\frac{M}{2\pi RT_2}} / \rho \quad (6)$$

where  $\Delta H_s$  is the latent heat associated with the vaporization of a solid below its melting point (cal/g),  $\rho$  is the density of the crystal (g/cm<sup>3</sup>), M is the molecular weight of the vapor (g/mole), and R is the gas constant (cal/(K·mole)). Equation (6) indicates that the growth rate of PVT method can be controlled by adjusting the temperature difference at two ends of the ampoule. Normally inert gases (N<sub>2</sub>, Ar) are infused into the ampoule after vacuum treatment to assist the nucleation of PVT crystal growth.<sup>21-23</sup> Since PVT growth is carried out at temperature much lower than the melting point of the material, it has multiple benefits of<sup>24</sup>: (a) reduced diffusion of impurities from containers, (b) reduced defects such as voids and dislocation densities, and (c) effective separation of impurities with low vapor pressure during transport. The major drawbacks for PVT methods are small crystal volume and uncontrolled nucleation. In practice, unless there is a large temperature gradient near the cooler end of the ampoule, multiple nucleations occur and the products at the cooler end are needles, platelets, or polycrystalline formed by many small crystals.

### 1.3 Modified Vertical Bridgman Growth

In this study, Bi<sub>3</sub> single crystals were mainly grown by a modified vertical Bridgman method. Pyrex glass ampoules were selected as the crystal growth containers since the annealing and softening points of the glass are 560°C and 815°C respectively, which are much higher than the maximum temperature (440°C) used in the growth of Bi<sub>3</sub> single crystal. The Pyrex glass tube was soaked in Decon Contrad® 70 for 12 hours to effectively remove the organics, rinsed 10 times with high purity DI water ( $\rho = 13.6 \text{ M}\Omega\text{-cm}$ ) and baked at 120°C for 12 hours. One end of the cleaned glass tube was melted and shaped to a sharp tip using a propane hand torch. Bi<sub>3</sub> powder (99.999%, MV Laboratories) was weighed and loaded in this tipped Pyrex glass ampoule. The ampoule needs to be evacuated and sealed to get rid of the water and oxygen as Bi<sub>3</sub> will react with them at elevated temperature. To do that, the ampoule was first vacuumed to a pressure of approximately  $4 \times 10^{-5}$  mbar. Heat was then gently applied on the ampoule wall using a propane hand torch to help evaporate the water. This step has to be done very carefully to avoid heating up the Bi<sub>3</sub> powder. Ar gas was then back filled in the ampoule to ~700 mbar. The purpose of infusing Ar gas is to make sure any residual gas after vacuum is inert. The cycle of pumping down, heating ampoule wall, and backfilling Ar gas was repeated three times, the final evacuation took around another 2-3 hours to take the pressure down to  $10^{-6}$  mbar. The ampoule was then sealed using a propane hand torch. To help seal the ampoule, a neck area was

preformed in air before the ampoule was pumped down. As the soft glass will collapse inwards due to the inner vacuum, the neck area will help the glass collapse into the opposing wall without breaking the seal. After sealing, the ampoule was vertically fixed in a standing frame and placed in a programmable 24 heating zone furnace (EDG-13, Mellen Company). The length of each heating zone is one inch and the temperature of each heating zone can be independently controlled by a computer program, which allows a precisely controlled temperature profile along the vertical axis of the furnace. The powder was first heated and kept at 440°C for 24 hours then cooled to 420°C at a rate of 10°C/h. The temperature profile was programmed to move up along the vertical axis with a fixed rate. This simulated the downward movement of the ampoule in the conventional vertical Bridgman method. The set up of this modified Bridgman system provides two advantages over the conventional one. First, possible vibration during crystal growth is eliminated since the ampoule is kept static in the new system. Second, a hole is no longer needed at the top of the furnace to provide the pass way for the hanging wire. Thus, less thermal disturbance is expected. As a result, the modified Bridgman system can provide a more stable crystal growth environment leading to better crystal qualities.

As discussed previously, temperature gradient and growth rate are two critical parameters for crystal growth by vertical Bridgman technique. The best way to start the crystal growth is to assess the relationship between the growth rate and temperature gradient at solid-liquid interface established in equation (1). However, it is difficult to do that in the case of  $\text{BiI}_3$  due to the unavailability of its thermal conductivity values. This is probably because  $\text{BiI}_3$  will dissociate to Bi and  $\text{I}_2$  at 250°C – 300°C,<sup>25</sup> and  $\text{I}_2$  is very corrosive with extremely high reactivity to metals, which could destroy the instrument for the thermal conductivity measurement. Therefore, in this study, different growth rates and temperature gradients for growing crystals with 0.75 inch diameter were investigated on an educated initial guess basis. Previous studies reported that  $\text{BiI}_3$  single crystals have been grown at the conditions of 1 mm/h growth rate with 15°C/cm temperature gradient<sup>1</sup> and 1 mm/h growth rate with 5.7°C/cm temperature gradient.<sup>2</sup> As equation (4) indicates that the temperature gradient depends on the thermal properties of the furnace,  $\text{BiI}_3$  single crystal grown in different furnaces could have very different temperature gradient. The highest temperature gradient allowed in the EDG 24-zone furnace is around 18°C/cm. The temperature variation in each zone is controlled within  $\pm 0.5^\circ\text{C}$ , which corresponds to a gradient variation of  $\pm 0.2^\circ\text{C}/\text{cm}$ . The investigated temperature gradients were then selected as 5, 10, and 15°C/cm to make a distinct difference between them. For each temperature gradient, the crystal growth has been conducted at a speed of 0.5, 1, and 2 mm/h.

#### 1.4 Physical Vapor Transport Growth

For the PVT crystal growth, the Pyrex glass ampoule was cleaned using the same procedure described for the MVB growth. A charge of 5 g  $\text{BiI}_3$  powder was loaded into a cleaned ampoule with diameter of 0.75 inches. The work charge was first vacuumed to around  $4 \times 10^{-5}$  mbar and cleaned with ultra high purity grade Ar gas three times, then finally sealed with ultra high purity grade Ar at 700 mbar. Following the crystal growth

conditions used by Cuña *et al.*,<sup>21</sup> the ampoule end with  $\text{BiI}_3$  powder was placed at 310°C and the other end was placed at room temperature. The growth time was 7 days for 5 g of powder. After the growth, the furnace was cooled down at a rate of 1°C/min.

## **2. Crsytal Growth Results and Discussion**

### **2.1 MVB Crystal Growth**

#### **2.1.1 Determination of Temperature Profile**

The concept of vertical Bridgman growth is quite simple. The powder is first heated to the melting temperature and soaked for a period of time. Then the crystal growth is conducted under certain temperature gradient and moving rate. Finally the entire growth system is cooled back to room temperature. While the temperature gradient and growth rate are vital for producing high quality single crystals, the heat up and cool down cycles are also important for a successful growth run.

As the furnace thermocouples are located at the furnace wall while the growth ampoule is in the center, the temperature difference is presented between the zone temperature reading and the actual temperature of the ampoule. To determine this difference, the central temperature was recorded by a K-type thermocouple placed along the central axis of the furnace. It was observed that the central temperature was around 20°C higher than the temperature reading at the furnace wall. To ensure the complete melting of  $\text{Bi}_3$ , the highest temperature for the soaking period was set as 440°C. This is based on the fact that ideally  $\text{Bi}_3$  will melt at 408°C and the actual soaking temperature will be around 460°C.

The heating rate is not a major concern for  $\text{Bi}_3$  as the processing temperature is in the medium range and Pyrex ampoule has a very low thermal expansion coefficient ( $3.2 \times 10^{-6}/\text{°C}$ ). The only concern is to make sure that the furnace temperature does not go up too fast or too slow, as both conditions require additional time to reach thermal equilibrium. Experimentally, the heating rate has been tested at 1, 3, and 5°C/min. It was found that at 3 and 5°C/min heating rates the furnace temperature could not follow the set temperature. The temperature lags were of around 10 and 30°C for the heating rate of 3 and 5°C/min respectively. When the heating rate was lowered to 1°C/min, the furnace temperature completely followed the set point with  $\pm 1^\circ\text{C}$  variations. Based on the test result, the heating rate was set at 1°C/min for all the crystal growth runs.

After the furnace reached the maximum temperature, the powder in the growth ampoule may still be lower than this point since heat transfer takes time. A soak period has to be set up to allow every component inside the furnace reach the thermal equilibrium. A K-type thermal couple was attached at the outer wall of the ampoule to test the equilibrium time. It was observed that the temperature was stabilized in the first 30 minutes after reaching the maximum temperature. However, the  $\text{Bi}_3$  melt inside the ampoule may need longer time to reach thermal equilibrium. A soaking time of 12 hours will be safe enough to thermally stabilize the whole growth system.

After soaking, the furnace was cooled down to 410°C at a rate of 1°C/min. The corresponding central temperature was around 430°C. This is to make sure the overall

furnace temperature is still above the melting point of  $\text{BiI}_3$ . Starting from this point, the crystal began to grow at a specific growth rate and temperature gradient described previously. The temperature at which the crystal growth ends is another important parameter needed to be determined. If the crystal growth ends at a high temperature, lattice disorder may happen due to the fast cooling of the atoms with high kinetic energies. On the other hand, ending the crystal growth at a very low temperature is time wasting. It is noted that the crystal growth of  $\text{BiI}_3$  by PVT method happens at  $\sim 250^\circ\text{C}$ ,<sup>4</sup> which implies that atoms at this temperature barely have enough kinetic energies to move around. Therefore, in this study, the crystal growth was set to end at  $200^\circ\text{C}$ , which corresponds to a furnace temperature of  $180^\circ\text{C}$ . The crystal after growth was cooled to room temperature at a rate of  $1^\circ\text{C}/\text{min}$ . A temperature profile was created based on the above discussion, as illustrated in Figure 3. The total growth time varies with the temperature gradient and growth rate. For example, the growth time for a crystal grown at  $10^\circ\text{C}/\text{cm}$  and  $0.5 \text{ mm/h}$  is around 20 days.

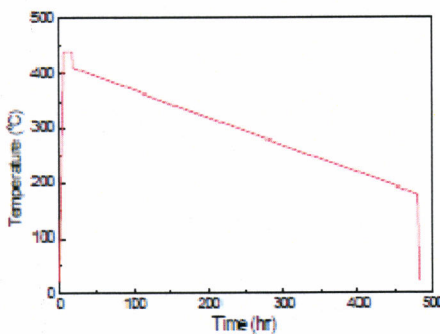


Figure 3. Growth recipe for the  $\text{BiI}_3$  crystal growth at  $10^\circ\text{C}/\text{cm}$  and  $0.5 \text{ mm/h}$ .

### 2.1.2 Crystal Growth Result

For crystal growth in 0.75 inch diameter ampoules, it was determined that only three different combinations of growth rates and temperature gradients produced large single crystals:  $10^\circ\text{C}/\text{cm}$  and  $0.5 \text{ mm/h}$ ;  $10^\circ\text{C}/\text{cm}$  and  $1 \text{ mm/h}$ ; and  $15^\circ\text{C}/\text{cm}$  and  $0.5 \text{ mm/h}$  (Table 1). The typical polycrystalline rods and cleavage planes of crystals obtained at different growth conditions are shown in Figure 4.

Table 3-1. Growth conditions for  $\text{BiI}_3$  single crystals in 0.75" diameter ampoules.

	Temperature Gradient ( $^\circ\text{C}/\text{cm}$ )			
	5	10	15	
Growth Rate (mm/h)	0.5 1 2	Polycrystalline Polycrystalline Polycrystalline	Single crystal Single crystal Polycrystalline	Single crystal Polycrystalline Polycrystalline

It is noticed that single crystals were obtained at the same temperature gradient ( $10^\circ\text{C}/\text{cm}$ ) but different growth rates ( $0.5$  and  $1 \text{ mm/h}$ ) or the same growth rate ( $0.5 \text{ mm/h}$ ) but different temperature gradients ( $10$  and  $15^\circ\text{C}/\text{cm}$ ). It is therefore clear that

equation (1) cannot explain these experimental results. However, one has to keep in is established on the steady state condition. A real crystal growth always happens at a non-steady state, although it may be very close to a steady state. Therefore, the requirement for crystal growth becomes

$$\rho_s L R < K_s G_s - K_L G_L \quad (7)$$

which suggests as long as the overall heat flux flowing away from the growth interface exceeds the rate of latent heat evolution, the growth of single crystal could happen.<sup>6</sup> This explains why  $\text{Bi}_3$  single crystals were obtained at the three conditions listed in Table 1.

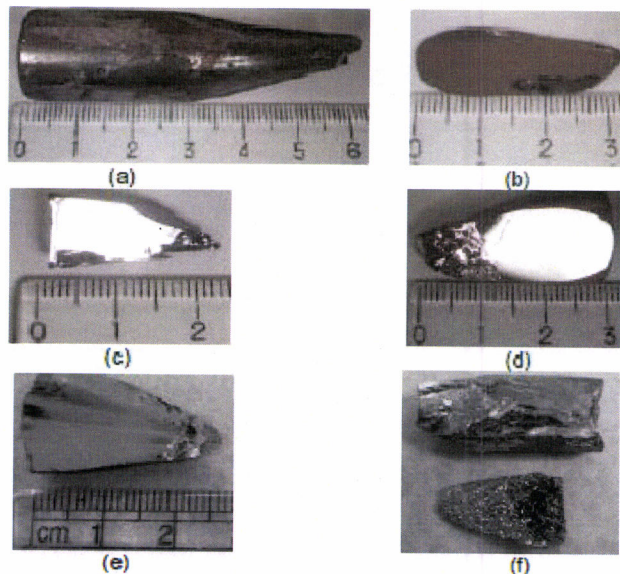


Figure 4. Single crystals produced by MVB method, (a) as grown polycrystalline rod; (b) crystal grown at  $10^\circ\text{C}/\text{cm}$  and  $0.5 \text{ mm/h}$ ; (c) crystal grown at  $10^\circ\text{C}/\text{cm}$  and  $1.0 \text{ mm/h}$ ; (d) crystal grown at  $15^\circ\text{C}/\text{cm}$  and  $0.5 \text{ mm/h}$ ; (e) crystal grown at  $15^\circ\text{C}/\text{cm}$  and  $1.0 \text{ mm/h}$ ; (f) polycrystalline cross section obtained at rest conditions.

Based on the above discussion, single crystals should also be grown at  $15^\circ\text{C}/\text{cm}$  and  $1 \text{ mm/h}$  given that single crystal was obtained at  $10^\circ\text{C}/\text{cm}$  and  $1 \text{ mm/h}$ . Actually, the solidification at this condition was characterized by parallel growth of multiple crystals, which had a non-smooth growth interface, as shown in Figure 3-7e. A possible reason for this kind of interface morphology was the thermal fluctuations at the growth interface, a phenomenon that has been commonly observed for other single crystal growths.<sup>26-28</sup> The growth furnace was observed to have a temperature fluctuation of around  $\pm 1^\circ\text{C}$  at a temperature gradient of  $15^\circ\text{C}/\text{cm}$ , compared to  $\pm 0.5^\circ\text{C}$  at a temperature gradient of  $10^\circ\text{C}/\text{cm}$ . A higher growth rate would cause more fluctuations and non-smooth interface compared to a lower growth rate. Therefore, crystal grown at  $15^\circ\text{C}/\text{cm}$  and  $1 \text{ mm/h}$  was

under a condition with high thermal fluctuations, which caused the formation of a non-smooth interface. By decreasing the temperature gradient to  $10^{\circ}\text{C}/\text{cm}$  or the growth rate to  $0.5 \text{ mm/h}$ , the thermal fluctuations were suppressed and smooth growth face was obtained. Based on the experimental results, the critical conditions to grow  $\text{BiI}_3$  single crystals with a diameter of  $0.75 \text{ inch}$  can be concluded as a temperature gradient between  $10^{\circ}\text{C}/\text{cm}$  and  $15^{\circ}\text{C}/\text{cm}$ , and a growth rate between  $0.5 \text{ mm/h}$  and  $1 \text{ mm/h}$ . A single crystal with a dimension of  $18 \times 13 \times 5 \text{ mm}^3$  has been successfully grown at the temperature gradient of  $10^{\circ}\text{C}/\text{cm}$  and growth rate of  $0.5 \text{ mm/h}$ , as shown in Figure 5.



Figure 5.  $\text{BiI}_3$  single crystal with dimension Of  $18 \times 13 \times 5 \text{ mm}^3$ , the largest crystal size ever reported.

This is the largest crystal size ever reported for  $\text{BiI}_3$ . The previously reported largest  $\text{BiI}_3$  single crystal had a dimension of  $12 \times 12 \times 4 \text{ mm}^3$ .<sup>29</sup>

### 2.1.3 PVT Crystal Growth

The growth ampoule and a single crystal platelet obtained after PVT growth are shown in Figure 6. Many tiny crystals, needles, and platelets were found to stack up together in the ampoule where the temperature was measured to be around  $230^{\circ}\text{C}$ , which was determined to be the growth temperature of the single crystal platelets. The platelets were carefully separated from the polycrystalline mixture by using tweezers and a razor blade. The typical platelet has a surface area of  $5 - 20 \text{ mm}^2$  and a thickness of  $100 - 200 \mu\text{m}$ .

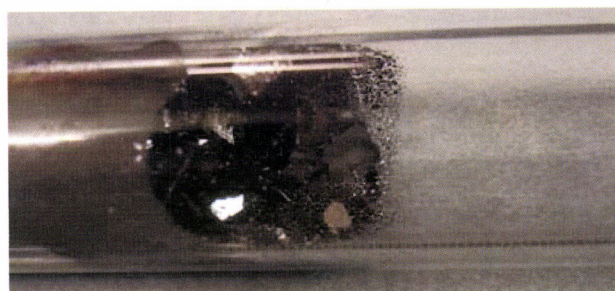


Figure 6.  $\text{BiI}_3$  single crystals grown by the PVT method.

### **3.0 Crystal Characterization**

A polycrystalline ingot was obtained after the crystal growth by the MVB method. Single crystal samples were cut from the ingot along the cleavage plane (001) with various cross sectional areas and thicknesses. For crystal grown by the PVT method, single crystal platelets with various dimensions were carefully collected. Single crystal samples obtained from both methods were characterized by the following techniques.

#### **3.1 Characterization Techniques**

##### **3.1.1 X-ray Diffraction**

X-ray diffraction using CuK $\alpha$  radiation (Philips APD 3720) was used to determine the crystallinity and phase purity of BiI<sub>3</sub> single crystals. The power of the X-ray generator was set to 40 kV and 20 mA. The 2 $\theta$  angle was scanned from 10° to 60° with a step size of 0.02°.

##### **3.1.2 Vickers Hardness**

The Vickers hardness of the grown single crystals was measured by a micro hardness tester (Buehler MicroMet II). Each sample was measured for 5 indentations and the applying force was 50 g.

##### **3.1.3 Etch Pit Density**

The dislocation density of the crystal surface was examined by EPD measurement using a KI solution as the etchant. To determine the ideal etchant concentration for EPD measurement, single crystal samples were etched in 5%, 10%, 15%, and 20% weight percent of KI solution respectively, and the etching time varied from 10 sec to 150 sec. After etching, the sample was rinsed with acetone and dried at 120°C for 10 min. The etched sample was weighed to determine the weight loss per unit surface area. The time dependence of the weight loss was calculated for each etchant concentration. The ideal etchant concentration was determined at which the etchant can effectively remove the mass of BiI<sub>3</sub> single crystal. After that, BiI<sub>3</sub> single crystals grown by the MVB and PVT methods were etched for a specific time. The density of pits was examined by an optical microscope (Nikon Eclipse LV100). For each sample, five randomly selected areas were studied to count the EPD.

##### **3.1.4 X-ray Rocking Curve**

The quality of the grown crystals was inspected by X-ray rocking curve on a Philips analytical MRD X'Pert System, as shown in Figure 7. The presence of defects such as dislocations and small angle grain boundaries will cause local variation of lattice spacing or plane orientation. For X-ray diffraction in the vicinity of a defect, Bragg's law cannot be simultaneously satisfied by the perfect lattice and the distorted one, which causes the broadening of X-ray diffraction peak. By performing X-ray rocking curve analysis,

the peak broadening of a specific lattice plane can be measured by scanning the incident angle  $\omega$  at a fixed receiving angle  $2\theta$ , as illustrated in Figure 8. The full width at half maximum (FWHM) of this peak is generally used to evaluate the quality of a single crystal.<sup>30-32</sup> The rocking curve  $\omega$ -scan was conducted at a rate of 0.002°/s with a step size of 0.001°. Each sample was scanned twice by rotating the sample 90° ( $\phi$  angle in Figure 8) relative to the previous scan, as illustrated in Figure 9.

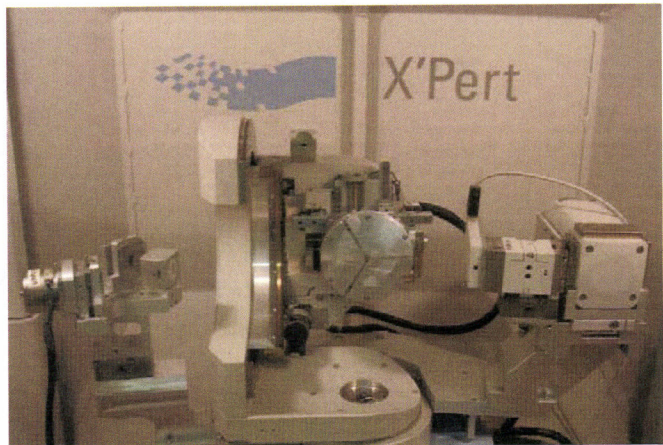


Figure 7. X'Pert system for X-ray rocking curve measurements.

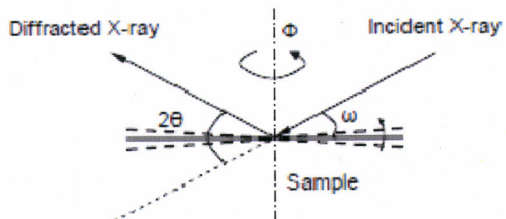


Figure 8. Illustration of rocking curve  $\omega$ -scan.

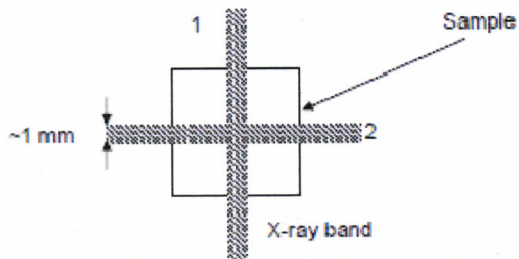


Figure 9. Illustration of the sampling for rocking curve  $\omega$ -scan. The shadowed bands numbered 1 and 2 represent the x-ray incident area for each scan.

### **3.1.5 Scanning Electron Microscopy (SEM)**

The surface microstructure of the as grown  $\text{BiI}_3$  single crystals was characterized using SEM (JEOL 6335F). The freshly cleaved surface was sputtered with carbon film with thickness of around 20 nm. The SEM was operated with an accelerating voltage of 15 kV, a probe current of 10  $\mu\text{A}$ , and a working distance of approximately 15 mm.

### **3.1.6 Atomic Force Microscopy (AFM)**

To study the surface morphology of the metal contacts, the sample surfaces were examined by AFM (Asylum Research AFM). The AFM tip from Veeco has a triangular cantilever and a nominal tip radius of 20 nm. The normal stiffness of the tip cantilever is 0.58 N/m. The topography images were acquired in contact mode at a fixed applied load of several nano Newton.

### **3.1.7 X-ray Photoelectron Spectroscopy (XPS)**

The stoichiometry of the grown  $\text{BiI}_3$  single crystal is determined by XPS spectrometer using an Omicron XPS system. The XPS spectra were collected from a freshly cleaved  $\text{BiI}_3$  crystal surface with an Al K $\alpha$  monochromatic X-ray (1486.7 eV). The spectra were recorded at a sampling area of 1.3 mm<sup>2</sup> and a take-off angle of 55° with pass energy of 22 eV (step size 0.05 eV, integration time 1 sec). The chamber pressure was kept below  $5 \times 10^{-10}$  mbar during measurement. The instrument resolution was around 0.1 eV. The peak energies were calibrated using a Ag 3d<sup>5/2</sup> peak at 368 eV. The composition of bismuth and iodine was estimated by comparing the photoelectron peak intensities of the Bi 4f with the I 3d core level peaks.

### **3.1.8 X-ray Fluorescence Spectroscopy (XRF)**

The stoichiometry of the grown single crystal was also determined by XRF using an Orbis Micro-XRF spectrometer (EDAX Inc.). The XRF spectrometer was operated using a Rh tube at 30 kV. The spot size of the X-ray was 30  $\mu\text{m}$ . The composition of bismuth and iodine was estimated by comparing the X-ray intensities of the Bi M-line with the I L-line in the measured spectrum.

## **3.2 Results and Discussion**

### **3.2.1 Crystal Structure and Phase Purity**

X-ray diffraction was used to determine the crystal structure and phase purity of single crystals grown by the two techniques described before. All the diffraction patterns were almost identical and a typical XRD pattern is shown in Figure 10. Only 003, 006, 009, and 0012 reflections parallel to the (001) plane were observed, and the peak positions matched well with the published  $\text{BiI}_3$  powder diffraction data for a rhombohedral crystal structure (JCPDS PDF# 48-1795).<sup>29</sup>

The lattice parameters of the single crystal grown by the MVB method were determined by performing  $2\theta$  scans on several selected planes. The scan was conducted by rotating and tilting the single crystal to satisfy the Bragg's condition for a specific plane that is not parallel to the crystal surface. The planes and their corresponding  $2\theta$  angle are listed in Table 3-2. The lattice parameters were calculated by least squares fit with values of  $a = 7.516 \pm 0.002 \text{ \AA}$  and  $c = 20.697 \pm 0.003 \text{ \AA}$ , which matched well with the published powder diffraction data of  $a = 7.519 \text{ \AA}$  and  $c = 20.721 \text{ \AA}$ .<sup>10</sup> The XRD results verified that  $\text{BiI}_3$  single crystals have been successfully grown by the MVB and PVT methods.

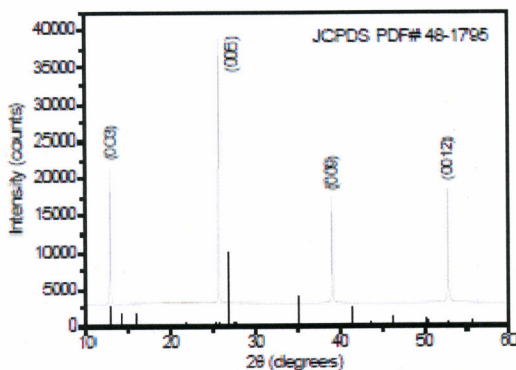


Figure 10. A typical XRD pattern for  $\text{BiI}_3$  single crystals.

Table 2.  $2\theta$  Angles of Selected Planes.

Planes (hkl)	003	104	107	116	018
$2\theta$	12.790	21.920	33.258	35.205	37.371

### 3.2.2 Vickers Hardness

Vickers hardness test is a method to determine the hardness of a material by measuring the size of an indentation produced under force by a pyramid shape diamond indenter.<sup>33</sup> The angle between the two opposite faces of the pyramid is  $136^\circ$ . After removal of the load, the two diagonals ( $d_1, d_2$ ) of the indentation on the surface of the material are measured under a microscope and their average is calculated (Figure 11). The area of the sloping surface of the indentation is calculated by

$$A = \frac{d^2}{2 \sin(136^\circ / 2)} \approx \frac{d^2}{1.8544} \quad (8)$$

where  $d$  is the mean diagonal of the indentation with a unit of mm. The Vickers hardness (HV number) is then determined by

$$HV = \frac{F}{A} \approx \frac{1.8544F}{d^2} \quad (9)$$

where F is the applied force with a unit of Kg.

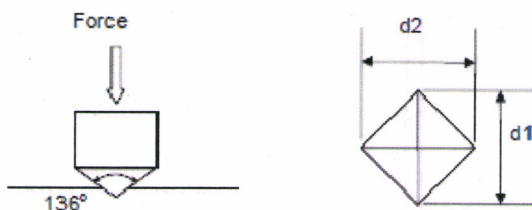


Figure 11. Illustration of the Vicker's hardness test.

The Vickers hardness on the (001) surface of single crystals grown by the MVB method was measured and is shown in Table 3. Single crystals grown by the PVT method were not subjected to the hardness test as the crystals are too thin. The average HV numbers of the single crystals grown at different conditions showed no significant difference. The results indicated that  $\text{BiI}_3$  single crystal is soft with a HV number between 12 and 15. As a comparison, the HV number of a  $\text{HgI}_2$  (001) surface is ~22,<sup>34</sup> a 316L stainless steel is 140.<sup>35</sup>

Table 3. Vickers hardness of (001) surface of  $\text{BiI}_3$  single crystals grown by the MVB method.

Meas.	10°C/cm, 0.5 mm/h			10°C/cm, 1 mm/h			15°C/cm, 0.5 mm/h		
	d1	d2	HV #	d1	d2	HV #	d1	d2	HV #
1	0.088	0.089	12	0.082	0.078	14	0.077	0.079	15
2	0.073	0.088	14	0.093	0.085	12	0.083	0.080	14
3	0.082	0.089	13	0.088	0.085	12	0.086	0.079	14
4	0.091	0.088	12	0.082	0.080	14	0.075	0.080	15
5	0.086	0.087	12	0.082	0.087	13	0.084	0.080	14
Aver.	13±0.15			13±0.16			14±0.18		

### 3.2.3 Etch Pit Density Measurement

The EPD measurement is generally utilized to determine the quality of semiconductor single crystals.<sup>36-38</sup> An etching solution is applied on the surface of a crystal and the etching rate increases at dislocation sites resulting in the formation of pits. Therefore, EPD is often used to evaluate the dislocation density of single crystals.<sup>39</sup> In this study, the etchant was KI solution as it was routinely used to reveal dislocations in  $\text{HgI}_2$ <sup>22</sup> and  $\text{PbI}_2$ .<sup>40</sup> The time dependence of the weight loss for different etchant concentrations is shown in Figure 12.

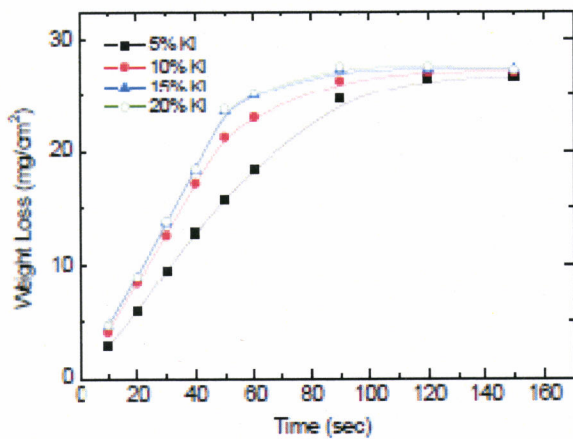


Figure 12.  $\text{BiI}_3$  etched in different concentrations of KI solution. The unit of weight loss is  $\text{mg}/\text{cm}^2$ .

It was observed that the initial etching rate increased with the etchant concentration. The weight loss reached a maximum after etching approximately 2 minutes for all solutions. The maximum weight loss was around  $27 \text{ mg}/\text{cm}^2$ , which corresponded to an etched depth of approximately  $50 \mu\text{m}$  for  $\text{BiI}_3$ . The weight loss curve showed almost no difference once the etchant concentration was higher than 15%. Therefore, 15% KI solution was selected as the etchant for the EPD study.

The optical images of  $\text{BiI}_3$  single crystal surfaces after etched in 15% KI solution are shown in Figure 13. The pits had a curved triangular shape, which represented the atomic arrangement of (001) plane. The size of the pits was around  $60 \mu\text{m}$  (the side length of the triangle) after etched for 10 sec. It was observed that the size of the pits increased with the increasing etching time. After etched for 30 sec, the pits started to overlap with each other and the number of pits became uncountable. Therefore the etching time for EPD measurements was determined to be 10 and 20 sec.

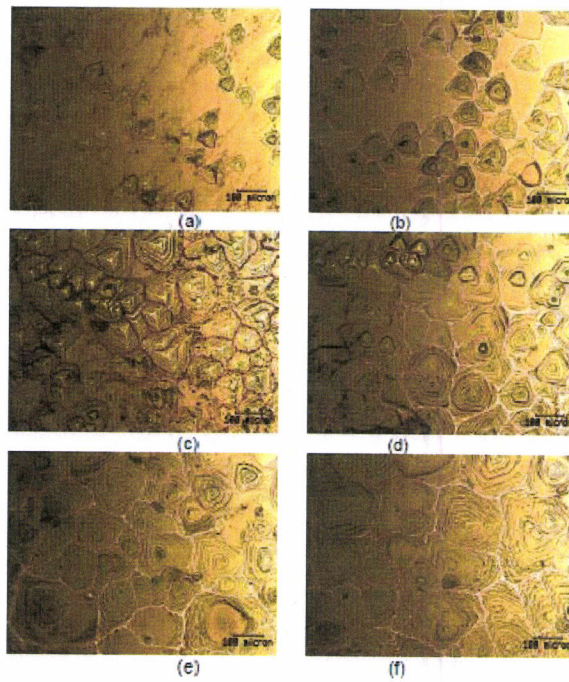


Figure 13. Optical images of the  $\text{BiI}_3$  single crystal surface after etched for time of (a) 10 sec; (b) 20 sec; (c) 30 sec; (d) 40 sec; (e) 50 sec; (f) 60 sec.

The typical images of etch pits for  $\text{BiI}_3$  single crystals are shown in Figure 14. No obvious etched pits were observed for crystals grown by the PVT method even when the etching time was extended from 10 to 60 sec. This indicated that crystals grown by the PVT method had much lower dislocation density than crystals grown by the MVB method.

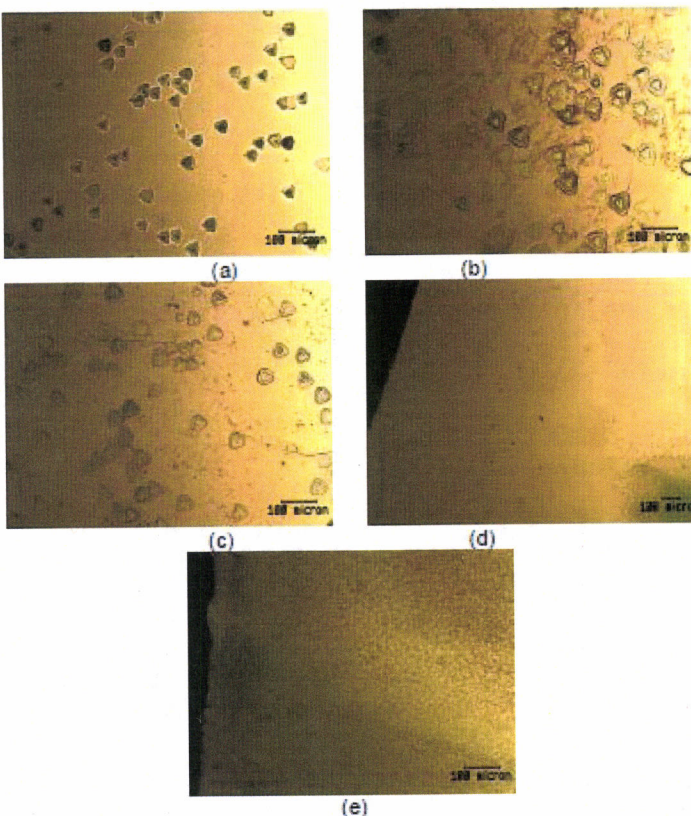


Figure 14. Etch pits of  $\text{BiI}_3$  single crystals grown by MVB and PVT methods. (a)-(c) MVB crystals grown at different conditions and etched for 10 sec; (d) PVT crystal etched for 10 sec; (e) PVT crystal etched for 60 sec.

When counting the number of the pits, if the pit crosses the corner of the area, it is counted as 1/4 pit; if the pit crosses the side, it is counted as 1/2 pit. The pit number was counted in an area of  $6.3 \times 10^{-3} \text{ cm}^2$ . The results of EPD measurements are summarized in Table 4.

Table 4. Etch pit density of single crystals grown by MVB method.

Growth condition	Etching time (s)	Number of pits					Average pit #	EPD ( $10^4 \text{ cm}^{-2}$ )
		Area 1	Area 2	Area 3	Area 4	Area 5		
$10^\circ\text{C}/\text{cm}$	10	65.50	60.25	81.50	77.00	68.50	70.55	$1.1 \pm 0.1$
$0.5\text{mm}/\text{h}$	20	83.00	72.50	76.00	76.50	82.25	78.45	$1.2 \pm 0.1$
$10^\circ\text{C}/\text{cm}$	10	87.25	73.50	105.50	88.00	95.50	89.95	$1.4 \pm 0.2$
$1\text{mm}/\text{h}$	20	91.50	82.50	87.00	97.25	85.50	88.75	$1.4 \pm 0.1$
$15^\circ\text{C}/\text{cm}$	10	85.00	80.25	95.50	71.25	83.50	83.1	$1.3 \pm 0.1$
$0.5\text{mm}/\text{h}$	20	102.50	86.00	93.50	88.00	77.50	89.5	$1.4 \pm 0.1$

It was observed that the number of pits varied from one area to another, which indicated the inhomogeneous distribution of dislocations in the MVB crystal. The EPD didn't show an apparent increase for a longer etching time (from 10 sec to 20 sec) and the extended time mainly increased the size of the pits, which is more obviously shown in Figure 13.

The EPD of  $\text{BiI}_3$  single crystals grown by the MVB method was on the order of  $10^4 \text{ cm}^{-2}$  and the crystal grown at  $10^\circ\text{C}/\text{cm}$  and  $0.5 \text{ mm/h}$  showed the smallest EPD. The EPD value of  $\text{BiI}_3$  is comparable with other semiconductor crystals such as  $\text{HgI}_2$  ( $\sim 10^3 - 10^5 \text{ cm}^{-2}$ )<sup>41-43</sup> and CZT ( $\sim 10^4 - 10^5 \text{ cm}^{-2}$ ).<sup>44-45</sup>

### 3.2.4 X-ray Rocking Curve

X-ray rocking curve characterization is a nondestructive analysis method compared to the EPD measurement. In this study, the X-ray rocking curves of  $\text{BiI}_3$  (006) plane were measured as this plane showed the highest intensity in X-ray diffraction (Figure 10). The X-ray rocking curve  $\omega$ -scans of  $\text{BiI}_3$  single crystals grown by MVB and PVT methods are shown in Figure 15. Features of extra peaks and shoulders were observed in all the crystals, which suggested that crystal planes in all these samples were not perfectly aligned. Defects such as dislocations and twin planes may account for these features. Multiple small crystals with orientation close to [001] may also exist in these crystals. The plot with log scale can reveal the low intensity features more clearly. The rocking curves scanned at two perpendicular directions for the same sample showed different shape and peak width. This indicated that the distribution of the defects was inhomogeneous in these crystals.

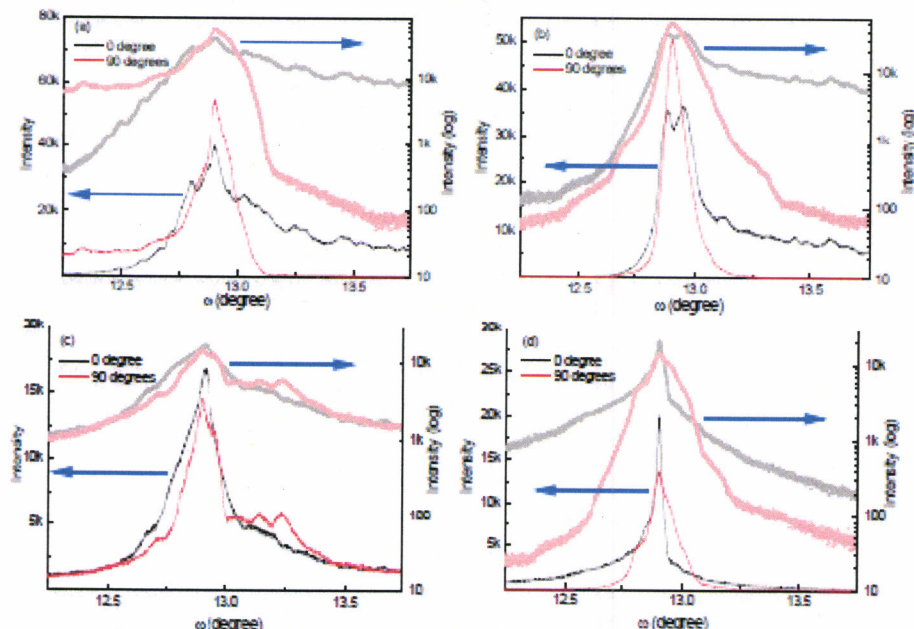


Figure 15. X-ray rocking curve  $\omega$ -scans of the single crystals. (a) – (c): single crystals grown by MVB at (a)  $10^\circ\text{C}/\text{cm}$  and  $1 \text{ mm/h}$ ; (b)  $10^\circ\text{C}/\text{cm}$  and  $0.5 \text{ mm/h}$ ; and (c)  $15^\circ\text{C}/\text{cm}$  and  $0.5 \text{ mm/h}$ . (d) Single crystal grown by PVT method. Solid line – linear intensity; circles – log scale intensity.

The FWHM of the rocking curves for each sample is summarized in Table 5. The crystals grown by MVB method showed similar rocking curve FWHMs thus the crystal quality could not be differentiated by this technique. On the other hand, the crystal grown by PVT method showed overall smoother peaks and smaller peak width

compared to the crystals grown by MVB method. This suggested that crystals grown by PVT method have better quality, which was in agreement with the EPD result.

Table 5 FWHM of X-ray rocking curves for  $\text{BiI}_3$  single crystals

	MVB Crystals 10°C/cm and 0.5 mm/h	10°C/cm and 1 mm/h	15°C/cm and 0.5 mm/h	PVT Crystal
0° scan	0.1818	0.3438	0.2292	0.0415
90° scan	0.1065	0.1670	0.1839	0.1181

The rocking curve  $\omega$ -2θ scan was performed on the MVB and PVT crystals to check the distribution of the (006) d-spacing, as shown in Figure 16. It was observed that the d-spacing distribution for both crystals had wide ranges, which could partially account for the broadening of the rocking curves.

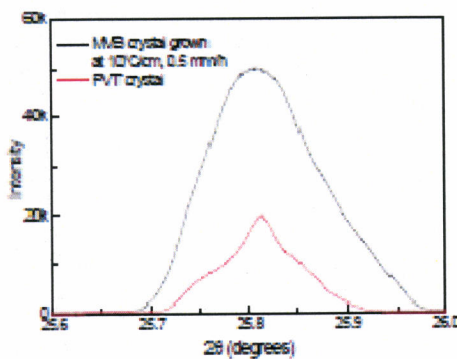


Figure 16. Rocking curve  $\omega$ -2θ scan of  $\text{BiI}_3$  single crystals indicated the wide distribution of d-spacing.

The poor crystalline perfection observed in  $\text{BiI}_3$  single crystals was also commonly observed in other iodine compound crystals such as  $\text{HgI}_2$  and  $\text{PbI}_2$ .<sup>46</sup> This was possibly due to the softness of all these materials. Strains induced from the thermal stress during the cooling of the crystal could easily cause the lattice distortion thus the broadening of the rocking curves. For  $\text{BiI}_3$  single crystal, similar FWHM values were also reported by Nason and Keller who grew the crystals on a seed using the PVT method. Their rocking curve measurement on (0012) plane showed FWHM values of 600 and 900 sec of arc, corresponding to  $0.17^\circ$  and  $0.25^\circ$  respectively.<sup>29</sup>

The rocking curves of  $\text{BiI}_3$  have exceedingly large FWHM values compared to other single crystals with similar EPD values. For example, a typical CZT crystal with  $\sim 10^4 \text{ cm}^{-2}$  EPD value exhibited a rocking curve FWHM of  $\sim 0.01^\circ$ .<sup>44</sup> A high quality GaAs crystal with EPD less than  $10^3 \text{ cm}^{-2}$  showed a rocking curve FWHM of  $\sim 0.001^\circ$ .<sup>47</sup> It should be noted that due to the softness of  $\text{BiI}_3$ , the crystal could also be deformed during cutting and handling, as evidenced in Figure 18. It is possible that the peak broadening was exaggerated by these additional strains.

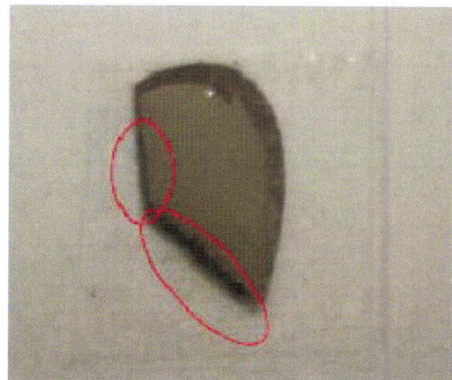


Figure 18. Deformation of  $\text{Bil}_3$  caused by cutting.

### 3.2.5 SEM Characterization

The (001) surface morphologies of  $\text{Bil}_3$  single crystal were observed by SEM. The surfaces were clean, smooth, and free of cracks, as shown in Figure 19. The deformation caused by cutting was clearly observed at the edge of the single crystal (Figure 19a). The layered structure of (001) planes was revealed in Figure 19b. The grey square box observed in Figure 19b was the evidence of surface damage caused by the strong electron beams, which illustrated the vulnerability of  $\text{Bil}_3$  to electrons.

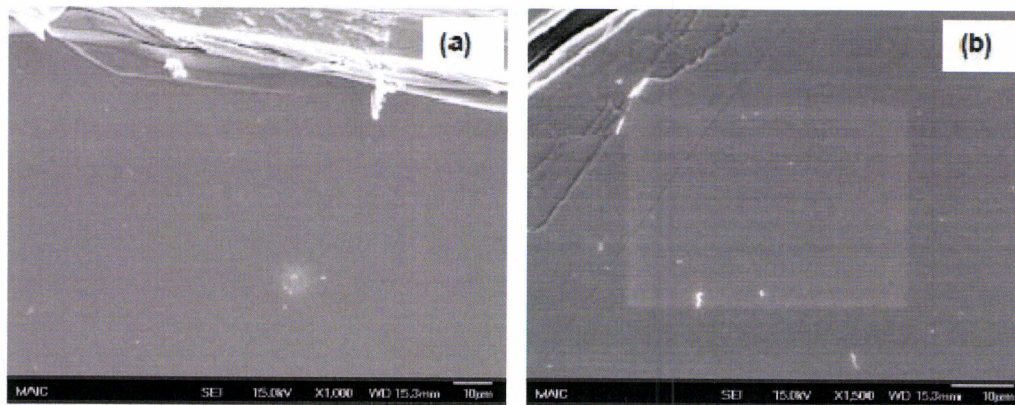


Figure 19. SEM images of  $\text{Bil}_3$  (001) surfaces show (a) deformation induced by cutting; (b) layered structure of (001) planes.

### 3.2.6 AFM Characterization

The topographic morphologies of the cleaved  $\text{Bil}_3$  surface were characterized by AFM. The surface was observed to be atomically rough with an average surface roughness of 0.484 nm (Figure 20).

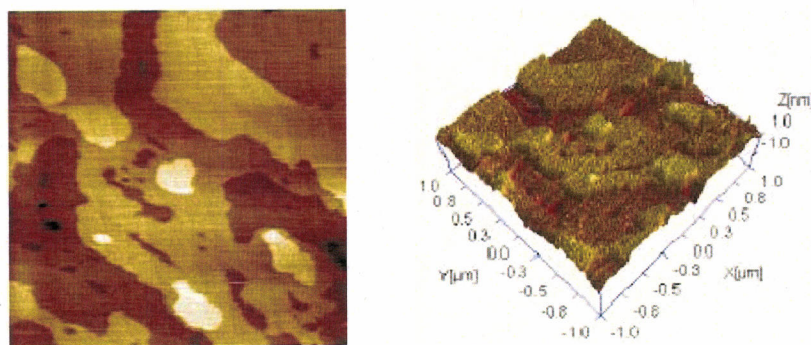


Figure 20. AFM images of  $\text{BiI}_3$  (001) cleaved surfaces.

The atomic layers were revealed in the topographic images with irregular edges, which was possibly due to the weak van der waal's forces between the layers along [001] direction.

### 3.2.7 XPS Characterization

The elemental composition near the surface of  $\text{BiI}_3$  single crystal was characterized by XPS. The full scanned XPS spectra are shown in Figure 21. On the freshly cleaved surface (1 day exposure in air), only carbon contamination was observed. For the surface with two weeks exposure in atmosphere, O 1s peak was clearly identified. The result suggested that  $\text{BiI}_3$  was stable in air for a short time, possibly several days. It will be eventually oxidized after a long time exposure in air. Therefore,  $\text{BiI}_3$  single crystals were stored in inert gas environment to avoid the oxidization.

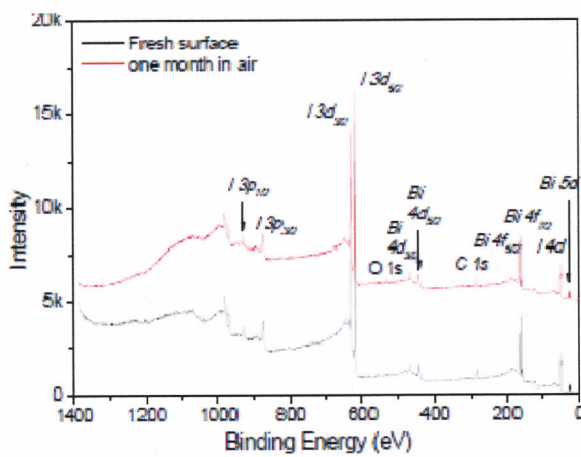


Figure 21. XPS spectrum of a freshly cleaved  $\text{BiI}_3$  single crystal.

The Bi 4f and I 3d spectra of the freshly cleaved surface were collected with higher resolution, as shown in Figure 22. The The I/Bi atomic ratio was calculated by the intensity ratio between the  $\text{I}^{3d^{5/2}}$  peak the Bi 4f peaks. The calculation indicated an iodine deficiency with I/Bi ratio of 2.78.

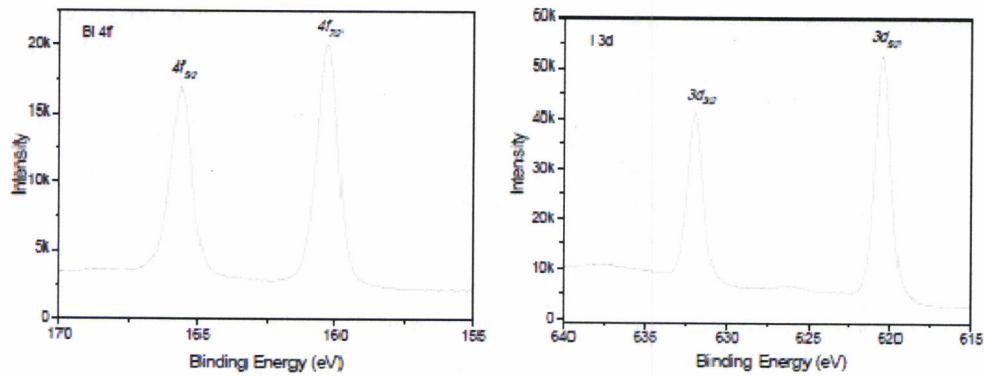


Figure 22. XPS spectra of Bi 4f and I 3d for a freshly cleaved  $\text{BiI}_3$  crystal surface.

### 3.2.8 XRF Characterization

The XRF spectrum of  $\text{BiI}_3$  is shown in Figure 23. Quantitative analysis was performed by comparing the intensities of Bi M-line to I L-line. The result indicated an I/Bi ratio of 2.54. Considering XRF is not a very sensitive analytical method, an uncertainty of ~10% is generally expected for the quantitative analysis.<sup>48-49</sup> The stoichiometry determined by XRF was consistent with the XPS characterization. Since XRF has a much higher sampling depth than XPS, the iodine deficiency is considered as the bulk defect of the single crystal.

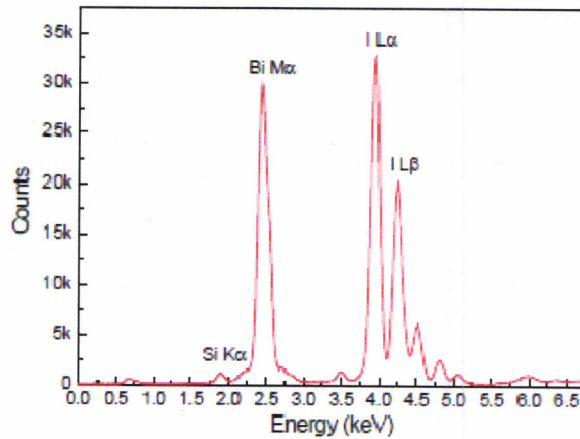


Figure 23. XRF spectrum of  $\text{BiI}_3$  on a freshly cleaved crystal surface.

The stoichiometric deviation of  $\text{BiI}_3$  single crystal was also observed by Matsumoto *et al.* who reported an I/Bi ratio of ~2.9 using XRF analysis.<sup>2</sup> The iodine deficiency issue has been commonly observed in other iodide semiconductor compound such as  $\text{HgI}_2$ <sup>50</sup> and  $\text{PbI}_2$ .<sup>51</sup> It was also reported that  $\text{BiI}_3$  tended toward dissociation into Bi and  $\text{I}_2$  at 250 – 300°C,<sup>5</sup> which implied that this stoichiometric deviation may come from the evaporation of iodine after crystal growth.

### 3.2.9 Determination of Band Structure

$\text{Bil}_3$  has been reported with different band gap characteristics and values. The experimentally and computationally determined band gap value of  $\text{Bil}_3$  was ranging from 1.59 eV to 2.2 eV as summarized in Table 6. For instance, Vashchenko and Timofeev measured the absorption spectra of  $\text{Bil}_3$  at room temperature and reported an indirect band gap of  $1.730 \pm 0.005$  eV.<sup>52-53</sup> Jellison *et al.* used two-modulator generalized ellipsometry to determine ordinary and extraordinary band gaps of  $1.991 \pm 0.005$  eV and  $1.997 \pm 0.002$  eV at room temperature.<sup>54</sup> Density functional theory (DFT) calculations by Schlüter *et al.* yielded a direct band gap of ~2.2 eV.<sup>55</sup> However, more DFT calculations by Yorikawa and Muramatsu suggested that  $\text{Bil}_3$  has an indirect band gap of approximately 1.59 eV with a rhombohedral crystal structure.<sup>56</sup> The much smaller band gap value was ascribed to the well-known, endemic underestimation of band gaps by local density approximation (LDA) calculations. There thus appears to be a discrepancy in the electronic structure and band gap values reported for  $\text{Bil}_3$  in the literature.

Table 6. Reported  $\text{Bil}_3$  Bandgap Values.

Crystal growth method	Characterization method	Band gap nature	Band gap (eV)	T (K)
Theory	EPM	Direct	2.2	0
Theory	NCPP-LDA	Indirect	1.59	0
Vertical Bridgman	Optical absorption	Indirect	1.730	293
			1.922	85
			2.029	20.4
Vertical Bridgman	Optical absorption	Direct	1.72	298
Vapor transportation	Optical transmission		1.73	298
Vapor transportation	Ellipsometry		1.991	298
Vapor transportation	Optical reflection	Indirect	1.97*	286
			2.072*	77
			2.08*	6

\*value obtained as peak energy at fundamental absorption edge

In this study, the band gap at room temperature was characterized by measuring optical transmission and reflection spectra at the wavelength of 300 to 800 nm. The sample is a freshly cleaved single crystal with thickness of 0.9 mm. The light source was a Newport ARC lamp housing 66902. A parallel single wavelength light beam was generated through a CornerstoneTM 260, Newport monochromator and incident on the crystal surface at an angle of 3° to the crystal optic axis. The intensity of the incident, reflected and transmitted light was measured separately by a UV-silicon detector (Newport).

### 3.2.9.1 Band Gap Determined by Optical Spectra at Room Temperature

The UV-Vis transmission and reflection spectra were measured from 300 nm to 800 nm at room temperature, and are shown in Figure 24. The absorption coefficient  $\alpha$  was determined from the experimental spectra by solving the following equation:<sup>56</sup>

$$T = \frac{(1-R)^2 e^{-\alpha d}}{1 - R^2 e^{-2\alpha d}} \quad (10)$$

where T is transmittance, R is reflectance, and d is the sample thickness. The relation between the absorption coefficient  $\alpha$  and incident photon energy ( $h\nu$ ) can be written as.<sup>57</sup>

$$(\alpha h\nu)^{\frac{1}{n}} = A(n\nu - E_g) \quad (11)$$

where  $\alpha$  is the optical absorption coefficient,  $h$  is Planck's constant,  $\nu$  is frequency of the incident photon, and  $E_g$  is the optical band gap. The exponent n depends on the type of optical transition. For direct transition,  $n = 1/2$ ; for indirect transition,  $n = 2$ . In order to determine the nature of the band gap, both direct and indirect band gap relations were examined.

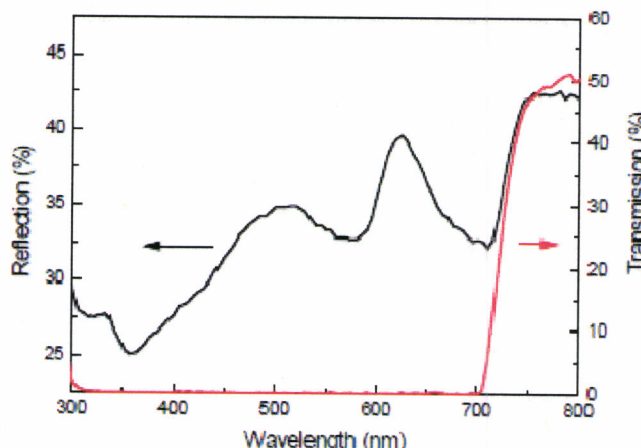


Figure 24. UV-Vis reflection and transmission spectra of  $\text{Bi}_3$ .

By plotting  $(\alpha h\nu)^2$  or  $(\alpha h\nu)^{1/2}$  versus  $h\nu$  and extrapolating the linear part to  $(\alpha h\nu)^2 = 0$  or  $(\alpha h\nu)^{1/2} = 0$ , the optical band gap was determined, as shown in Figure 25.

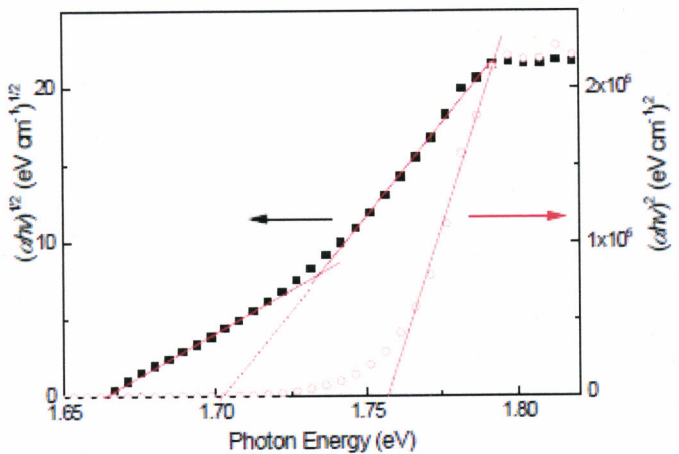


Figure 25. Behavior of  $(\alpha h\nu)^2$  or  $(\alpha h\nu)^{1/2}$  versus photon energy.

A stepped structure was observed in the  $(\alpha h\nu)^{1/2}$  versus  $h\nu$  plot, indicating an indirect band characteristic of  $\text{BiI}_3$ . The band gap value was determined by the average of the two interceptions at  $(\alpha h\nu)^{1/2} = 0$ , which gave an indirect band gap of  $1.68 \pm 0.09$  eV at room temperature. This value is in agreement with experimental value reported in references<sup>50,58-60</sup>, but smaller than the values reported in references<sup>51,61</sup>, as listed in Table 6.

### 3.2.9.2 Effect of Temperature on Band Gap

The effect of temperature on the band gap was determined by measuring UV-Vis transmission spectra from 298 to 330 K; the results are shown in Figure 26. It was observed that the absorption edge shifts to the lower energy side when the temperature is increased. The absorption coefficient  $\alpha$  was calculated assuming that the energy loss of the transmitted light was solely due to the sample absorption,

$$\alpha = -\frac{1}{d} \ln(T) \quad (12)$$

where  $d$  is the sample thickness and  $T$  is transmittance. The dependence of  $(\alpha h\nu)^{1/2}$  and  $(\alpha h\nu)^2$  on the photon energy is plotted in Figure 27.

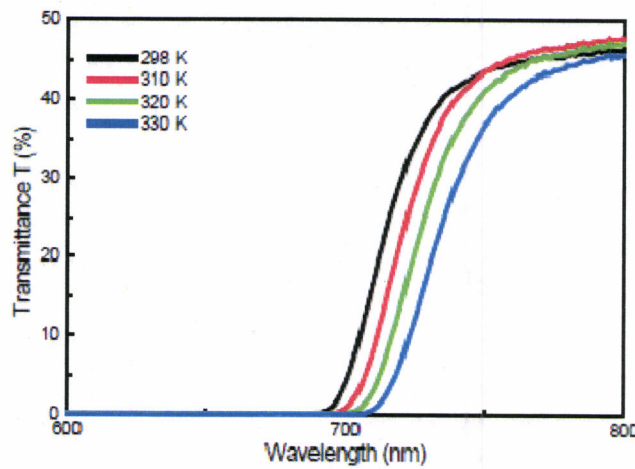


Figure 26. UV-Vis transmission spectra of a  $\text{Bi}_3$  single crystal at different temperatures.

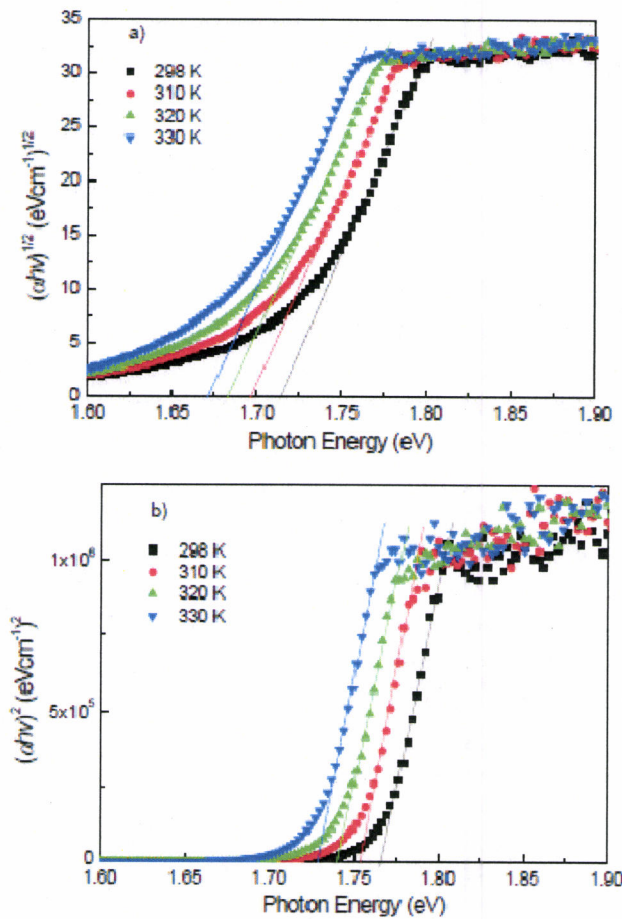


Figure 27. (a) Dependence of indirect band gap model on the photon energy; (b) dependence of the direct bandgap model on the photon energy.

Continuous curves instead of stepped characteristics are observed in the  $(\alpha h\nu)^{1/2}$  versus  $h\nu$  plot, which indicate that the gap is not indirect band. However, it is important to note that compared with the optical spectra, here the reflectance was not taken into account for the calculation of absorption coefficient. This is particularly relevant because equation 11 is only valid for a sample with negligible reflectivity, which is not the case here given the mirror surface of the  $\text{BiI}_3$  single crystals investigated here. Therefore, this simplified solution of absorption coefficient will not truly represent the band gap characteristics of  $\text{BiI}_3$  as key features may be lost in the  $(\alpha h\nu)^{1/2}$  versus  $h\nu$  plot when  $\alpha$  approaches zero.

Nevertheless, it is clearly observed that in the UV-Vis transmission spectra the absorption edge of  $\text{BiI}_3$  red-shifts with increasing temperature (Figure 26). The temperature coefficient between 298 and 330 K was calculated based on the plot in Figure 27a and the value is about  $-1.18 \times 10^{-3}$  eV/K. This temperature effect has also been reported by other researchers, as indicated in Table 4-1. This red-shifting of the band gap with temperature has been generally found in many semiconductor materials.<sup>62-64</sup> An empirical fit has been experimentally determined to describe the band gap as a function of temperature:<sup>65</sup>

$$E_g(T) = E_g(0) - \frac{\alpha T^2}{T + \beta} \quad (13)$$

where  $E_g(0)$  is the band gap at absolute temperature,  $\alpha$  and  $\beta$  are the fitting parameters. Fitting the data obtained from Figure 27a gives  $E_g(0) = 2.06$  eV,  $\alpha = 1.36 \times 10^{-3}$  eV/K and  $\beta = 52$  K. The band gap at absolute 0 K is then determined to be 2.06 eV, which is about 0.2 eV smaller than the theoretical value. If  $\alpha T/(T+\beta)$  is taken as temperature coefficient of the band gap, this coefficient increases with increasing temperature. Different temperature coefficients with close values have been reported for  $\text{BiI}_3$ . For example, Komatsu and Kaifu obtained temperature coefficient of  $-1.8 \times 10^{-4}$  eV/K between 6 and 77 K, and  $-3.4 \times 10^{-4}$  eV/K between 77 and 286 K. Vashchenko and Timofeev reported a coefficient of  $-9.2 \times 10^{-4}$  eV/K between 85 and 293 K. As a comparison, temperature coefficients of  $\text{BiI}_3$  were calculated using above fitted parameters and listed in Table 7.

Table 7. Temperature coefficient of  $\text{BiI}_3$  calculated based on the fitting parameters.

Temperature (K)	6	77	85	286	293
Temperature Coefficient (eV/K)	$-1.4 \times 10^{-4}$	$-8.1 \times 10^{-4}$	$-8.4 \times 10^{-4}$	$-1.2 \times 10^{-3}$	$-1.2 \times 10^{-3}$

It is shown that temperature coefficients obtained in this study have slightly higher values, yet the range of the values have good agreement with those reported previously.

### 3.2.10 Effects of Impurities on Band Gap

Band gap narrowing is an effect commonly observed in heavily doped semiconductor materials.<sup>66-68</sup> The physical mechanisms for band gap narrowing fall into two categories: dopant atoms interacting with the semiconductor and modifying its band structure, and strain introduced by the doping process.<sup>69</sup> The band gap narrowing effect has a general form of

$$\Delta E_g \approx AN^{\frac{1}{3}}, \quad (14)$$

where A is constant, and N is the dopant concentration.<sup>69</sup> For Si, the band gap narrowing is about 0.02 eV with  $10^{17} \text{ cm}^{-3}$  dopant concentration.<sup>70</sup> If the impurities in  $\text{BiI}_3$  single crystal are considered as an extrinsic dopant and the concentration is high, a similar band gap narrowing effect is expected.

The impurity levels of the  $\text{BiI}_3$  powder along with the crystals grown in Pyrex glass and quartz ampoules are reported in Table 8. The concentration was calculated based on the mole ratio between the impurity element and  $\text{BiI}_3$ . The concentration of Pb in the powder and crystals was below the detection limits of ICP-AES.

Table 8. Impurity Concentrations in  $\text{BiI}_3$  Powder and Crystals.

	Ag	Cu	Fe	Ni	Pb	Si
Raw powder	$3.4 \pm 0.60$	$0.8 \pm 0.02$	$7.1 \pm 1.86$	$0.1 \pm 0.01$	<1	$7.2 \pm 0.71$
Impurity concentrations of crystal grown in Pyrex glass ampoule						
Distance from the tip (mm)	Ag	Cu	Fe	Ni	Pb	Si
0	$2.2 \pm 0.57$	$0.3 \pm 0.01$	$5.5 \pm 0.05$	$0.2 \pm 0.01$	<1	$4.8 \pm 0.38$
5	$4.6 \pm 0.55$	$0.3 \pm 0.01$	$6.1 \pm 0.08$	$0.1 \pm 0.01$	<1	$6.5 \pm 0.46$
10	$2.4 \pm 0.10$	$0.5 \pm 0.01$	$6.0 \pm 0.24$	$0.2 \pm 0.01$	<1	$5.9 \pm 0.78$
15	$2.9 \pm 0.13$	$0.2 \pm 0.01$	$6.6 \pm 0.12$	$0.1 \pm 0.01$	<1	$6.3 \pm 0.53$
20	$1.3 \pm 0.03$	$0.2 \pm 0.01$	$4.3 \pm 0.18$	$0.1 \pm 0.01$	<1	$6.5 \pm 0.38$
25	$2.6 \pm 0.06$	$0.1 \pm 0.01$	$5.3 \pm 0.08$	$0.1 \pm 0.01$	<1	$4.6 \pm 0.34$
Impurity concentrations of crystal grown in quartz ampoule.						
0	$2.4 \pm 0.11$	$0.2 \pm 0.01$	$5.6 \pm 0.21$	$0.3 \pm 0.01$	<1	$4.2 \pm 0.15$
5	$2.0 \pm 0.17$	$0.2 \pm 0.01$	$4.2 \pm 0.11$	$0.3 \pm 0.02$	<1	$3.5 \pm 0.23$
10	$3.1 \pm 0.08$	$0.2 \pm 0.01$	$4.9 \pm 0.15$	$0.1 \pm 0.01$	<1	$4.7 \pm 0.36$

It was observed that the impurity concentrations of the grown crystal maintained the same level as  $\text{BiI}_3$  powder. The crystals grown in Pyrex and quartz ampoules had similar impurity concentrations, which suggested that crystal growth in Pyrex glass ampoule was sufficient to maintain the impurity level of the starting material. This is a great processing advantage given the easier ampoule vacuum sealing of Pyrex when compared to quartz.

The sum of the impurity concentrations for all the analytes were around 20 ppm in the crystal. Given that  $\text{Bi}_3$  has an atomic concentration of  $2.37 \times 10^{22} \text{ cm}^{-3}$ , 20 ppm impurity concentration was converted into an atomic concentration of  $4.74 \times 10^{17} \text{ cm}^{-3}$ . This was considerably high doping concentration if all the impurity elements were “doped” into the crystal. It was therefore reasonable to expect that the band gap of  $\text{Bi}_3$  crystal was narrowed by the impurities.

The impurity distribution in the crystal grown in Pyrex glass ampoule was uniform along the axis of the crystal ingot, as shown in Figure 28, which suggested that the impurities was hardly segregated during MVB crystal growth.

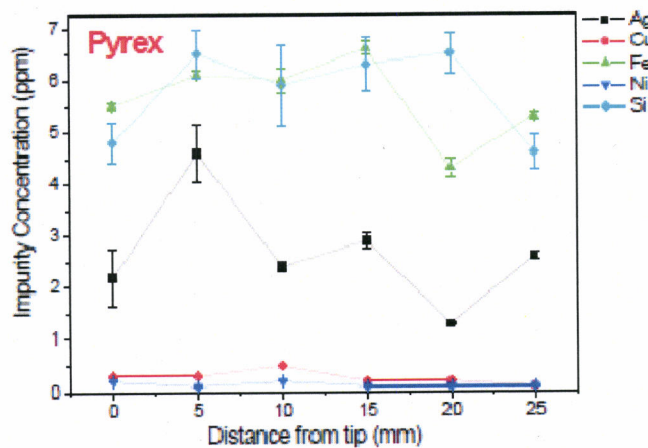


Figure 28. Impurity distribution along the  $\text{Bi}_3$  crystal grown in Pyrex ampoule.

The band gap measured at room temperature showed close value to most of the literature listed in Table 6 except for reference 39 and 71. Regarding to reference 71, one should be noted that the values were actually taken from the peak energy of the fundamental absorption edge, which should be higher than the intrinsic band gap as the value is taken at the maximum absorption coefficient  $\alpha$  instead of at  $\alpha$  approaching to zero. In other words, the values reported in reference 71 are related to band gap but with higher energy. They are not the true band gap values, but their change with temperature represents the temperature dependence feature of band gap.

The band gap in reference 39 was measured by ellipsometry. A comparison of spectroscopic ellipsometry and transmission and reflection spectroscopy measurements indicates the relative strengths and weaknesses of the two techniques. Spectroscopic ellipsometry has proven to be useful in extracting the material microstructure in the form of surface features, the index of refraction below the band gap, and the critical point features above the direct gap. This technique, however, lacks the sensitivity when the absorption coefficient is lower than  $\alpha \sim 10^4 \text{ cm}^{-1}$ . When the absorption coefficient is extracted using transmission and reflection spectroscopy, sensitivity is retained to  $\alpha \sim 10^2 \text{ cm}^{-1}$ . Transmission and reflection measurements generally lack sensitivity to the material microstructure, which can lead to erroneous assignment of the above-gap critical point transitions. A combination of these two techniques allows for the accurate

determination of the material microstructure and of the optical properties across the given spectral range. From reference 72, it is clearly apparent that when the band gap characteristics are above  $\alpha \sim 10^4 \text{ cm}^{-1}$  either technique is useful for extraction of the direct or indirect gap, but when the characteristics are lower than  $\alpha \sim 10^4 \text{ cm}^{-1}$  transmission and reflection measurements should be used. Thus the different band gap values obtained by UV-Vis and ellipsometry can be attributed to the different range of absorption coefficient used for the data fitting, which is determined by the nature of the techniques. In the case of  $\text{Bil}_3$ , UV-Vis is more accurate to determine the band gap as its band characteristics are lower than  $\alpha \sim 10^4 \text{ cm}^{-1}$ .

The decrease of band gap value due to increasing temperature and high impurity concentration has been observed in  $\text{Bil}_3$ . However, the effects are rather small, such that they cannot match the difference between experimental and theoretical values. Theoretical DFT calculation gave an indirect band gap value of 2.28 eV.<sup>72</sup> The experimentally determined value was 2.06 eV at zero temperature by fitting the data obtained from 298 to 330 K. The band gap narrowing caused by impurities has been theoretically studied using DFT calculation, which gave a 0.3 eV decrease of band gap for Cu impurity with concentration of  $\sim 10^{20} \text{ cm}^{-3}$ .<sup>72</sup> The theoretical study also showed that not every impurity element will cause the band gap narrowing of  $\text{Bil}_3$ . For instance, Si was observed to have no effect on the band structure modification. The band gap narrowing in  $\text{Bil}_3$  should be far less than 0.3 eV, since the impurity concentration in the crystal ( $\sim 10^{17} \text{ cm}^{-3}$ ) is much smaller than the value used in DFT calculation.

## **4. Detector Fabrication and Testing**

### **4.1 Detector Fabrication**

For detector fabrication, a metal electrode has to be deposited on the surface of  $\text{BiI}_3$ . The proper choice of the electrode materials is extremely important for the success of the detector. Au and Pd have both been used as electrode materials for  $\text{BiI}_3$  detectors.<sup>1</sup>

<sup>3</sup> However, the properties of the electrical contacts have never been reported. It is important to understand how the metal contact interacts with the substrate. The reactivity of the metal-semiconductor interface should be used as a guide for the selection of contact material. X-ray photoelectron spectroscopy (XPS) has been widely used to explore the metal-semiconductor interfaces with great success at explaining and predicting the reactivity of the interfaces.<sup>73-74</sup> In this study, different electrode materials of Au, Pd, and Pt have been sputter coated on the surfaces of  $\text{BiI}_3$  single crystals. The metal- $\text{BiI}_3$  interface has been studied by XPS and AFM. The resistivity of  $\text{BiI}_3$  single crystals with different contact materials have been measured and compared.

#### **4.1.1 XPS**

##### **4.1.1.1 Principles of XPS**

XPS is an electron spectroscopic method that uses monoenergetic soft X-rays to eject electrons from the inner shell orbitals of a sample and analyzes the energy of the detected electrons.<sup>75</sup> In this study, the X-ray source is a monoenergetic Al K $\alpha$  (1486.7 eV) X-ray. The kinetic energy of an ejected electron is given by

$$E_k = h\nu - E_b - \varphi_s \quad (15)$$

where  $h\nu$  is the energy of the photon,  $E_b$  is the electron binding energy which is the energy difference between the Fermi level and the energy of the atomic orbital from which the electron originates, and  $\varphi_s$  is the work function of the spectrometer. Since an atom has multiple orbitals, the corresponding photoelectron spectrum has a variety of peaks that are named according to the orbital ( $l = 0, 1, 2, 3\dots$ denoted as s, p, d, f...) and spin ( $s = 1/2$ ) quantum numbers. The total momentum of the photoelectrons ( $J = l + s$ ) is included in the labeling of a measured photoelectron peak (e.g., Bi 4f $^{7/2}$  where  $l + s = 3 + 1/2 = 7/2$ ). The electron binding energy of an element varies with different compounds due to the change of electronic environment. Therefore XPS can be used to identify the chemical state of the materials being analyzed. Since the energy of the X-ray source is low, the penetration depth of the photons is on the order of micrometers. Only those electrons that originate within tens of angstroms below the solid surface can escape the surface without appreciable energy loss, which makes XPS majorly used as a surface analytical technique.

##### **4.1.1.2 Sample Preparation for XPS**

The (001) surface of a  $\text{BiI}_3$  single crystal was cleaved in air by peeling off the top layer of the crystal using Scotch tape. The cleaved surface was sputtered with Au, Pd, and Pt metals with thickness of around 1 nm using Kurt J. Lesker CMS-18 multi target sputter system. The sputtering was conducted in a vacuum chamber with a pressure of  $10^{-8}$  torr at a deposition speed of around 0.5 nm/s at room temperature. A freshly cleaved surface of a  $\text{BiI}_3$  single crystal was used as a reference. X-ray photoelectron spectra were collected by an Omicron XPS system with an Al K $\alpha$  monochromatic X-ray (1486.7 eV). The spectra were recorded at a sampling area of  $1.3 \text{ mm}^2$  and a take-off angle of  $55^\circ$  with pass energy of 22 eV and step size 0.05 eV. The chamber pressure was kept below  $5 \times 10^{-10}$  mbar during measurement. The instrument resolution was < 0.1 eV. The peak energies were calibrated using a Ag 3d $^{5/2}$  peak at 368 eV. The studied elements included bismuth, iodine, gold, palladium, platinum, carbon, and oxygen.

#### **4.1.2 Atomic Force Microscopy (AFM)**

To study the surface morphology of the metal contacts, the sample surfaces were examined by AFM with an Asylum MFP-3DTM Research AFM. The AFM tip from Veeco has a triangular cantilever and a nominal tip radius of 20 nm. The normal force constant of the tip cantilever is 0.58 N/m. The topography images were acquired in contact mode at a fixed applied load of several nN.

#### **4.1.3 I-V Characterization**

The resistivity of  $\text{BiI}_3$  single crystals with different electrodes was studied by I-V characterization using an Agilent 4155B semiconductor parameter analyzer. Samples were prepared by sputtering Au, Pd, and Pt on the freshly cleaved surface resulting in an electrode thickness of ~200 nm. The sputtering was conducted at the same conditions as described for the XPS samples. Pt wires were attached to the electrodes using silver paste (SPI® Supplies) for electrical connection.

#### **4.1.4 Results and Discussion**

##### **4.1.4.1 The XPS Spectra**

The XPS core-level spectra of all the electrode elements detected are shown in Figure 29. The binding energies of each element in different compounds are given in Table 9.

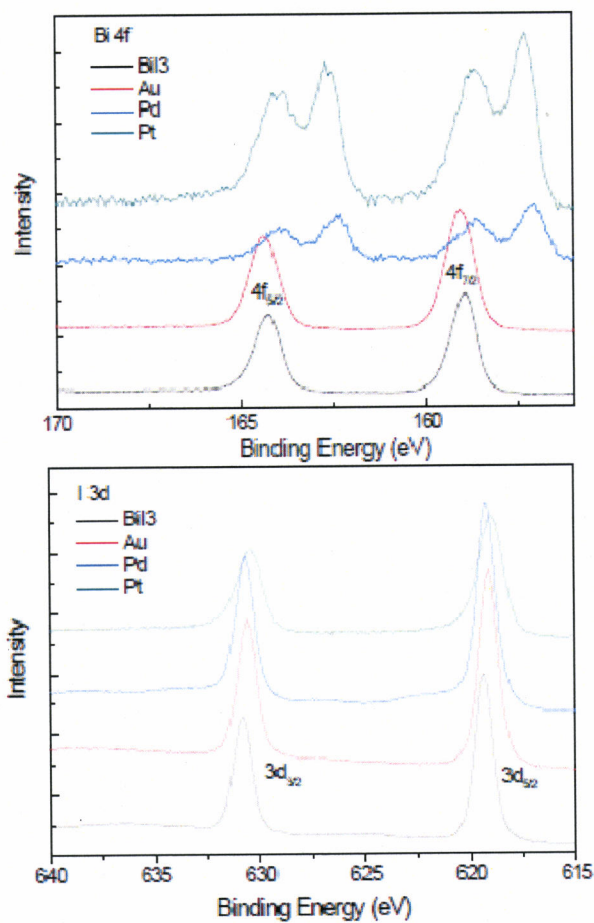


Figure 29. XPS spectra of Bi 4f and I 3d for the freshly cleaved  $\text{BiI}_3$  (001) surface and surface with Au, Pd, and Pt electrodes.

Table 9. Observed binding energies of the several elements observed within the XPS spectra.

Peak	$\text{BiI}_3$ sample	Binding energy (eV)			
		Au sample	Pd sample	Pt sample	
Bi 4f7/2	159.2	159.1	158.6	157.1	158.6
I 3d5/2	619.4	619.1	619.3		619.0
C 1s	284.7	284.6	284.0		284.3
O 1s		532.2	529.9	533.0	532.1
Au 4f7/2		84.0			
Pd 3d5/2			335.0	336.5	
Pt 4f7/2					71.1

In the following discussion, the sample without deposited metal is called  $\text{BiI}_3$  sample, and the samples with deposited metallic contacts are named Au, Pd, and Pt samples respectively. A quick survey of the XPS spectra reveals that the Au sample maintains the chemical environment of  $\text{BiI}_3$ , while Pd and Pt show interactions with the substrate. The detailed discussion for each sample is given in the following sections.

#### 4.1.4.2 Au Sample

The XPS spectra of the Au sample show peak positions of Bi 4f and I 3d very close to those of the  $\text{BiI}_3$  sample; and the Au 4f spectrum exhibits the same peak positions with that of a pure gold. The results suggest that Bi, I, and Au maintain their respective chemical state and there is no chemical interaction between Au and  $\text{BiI}_3$ . The C 1s and O 1s spectra are shown in Figure 30.

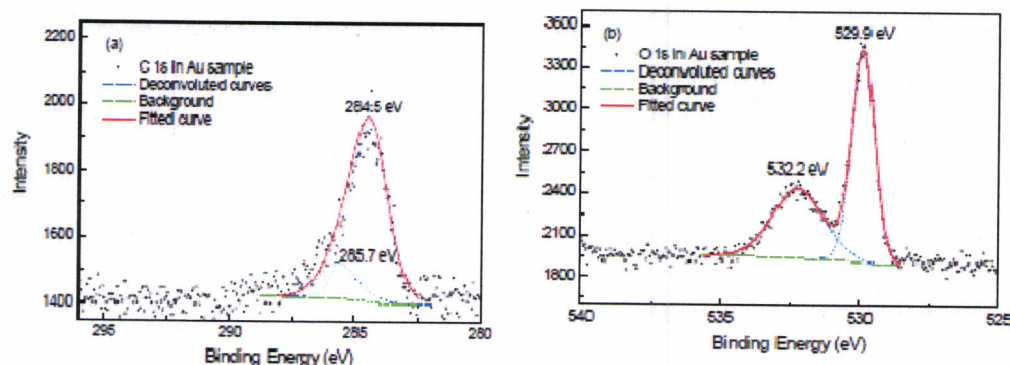


Figure 30. Deconvolution of XPS spectra for the AU sample peak (a) C 1s and (b) O 1s.

The C 1s spectrum of the Au sample can be deconvolved into two peaks with the peak at 284.5 eV assigned to amorphous carbon<sup>76</sup> and the peak at 285.7 eV assigned to carbon species bound to oxygen<sup>77-79</sup> (Figure 30a). Two distinct peaks are observed in O 1s spectrum (Figure 30b). The peak at 532.2 eV is attributed to oxygen atoms bound to carbon.<sup>77</sup> The peak at 529.9 eV could be assigned to oxygen atoms in  $\text{Au}_2\text{O}_3$  (530.2 eV)<sup>58</sup> or atomic O adsorbed at Au surface (530.2 eV).<sup>77</sup> Since there is no indication of any Au-O bond in the Au 4f spectrum, this peak is assigned to atomic O adsorbed at the Au surface.

#### 4.1.4.3 Pd Sample

Peak shifting of Bi 4f and Pd 3d is observed, which indicates the existence of an interfacial reactivity. The iodine peaks remain the same as the  $\text{BiI}_3$  sample. The deconvolution of Bi 4f, Pd 3d, C 1s, and O 1s spectra are shown in Figure 31. The properties of the fitted peaks and their assignments are summarized in Table 10.

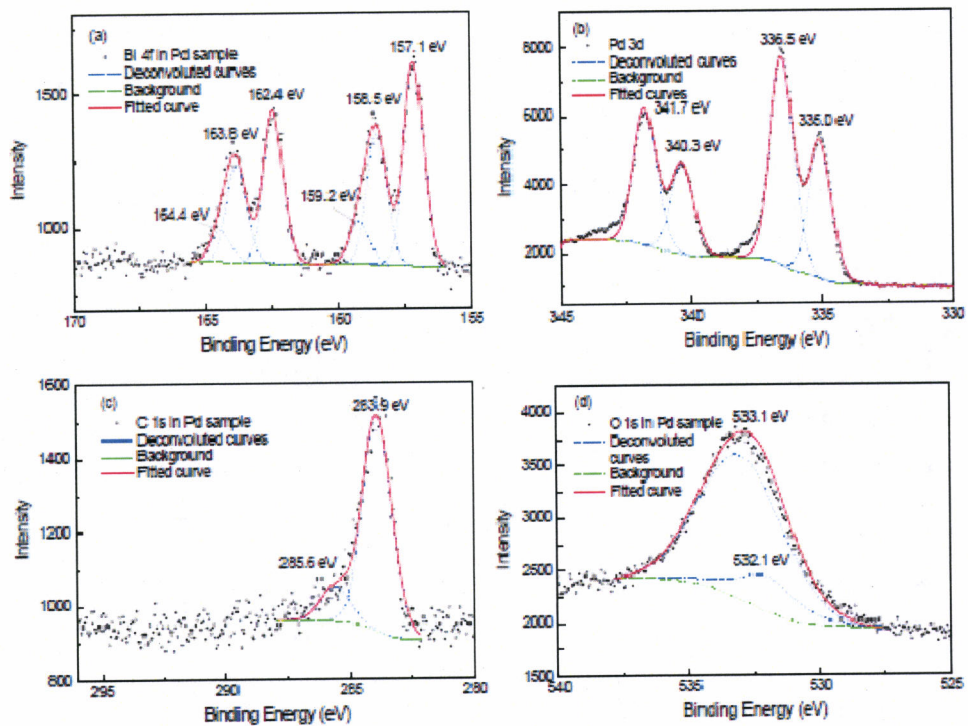


Figure 30. Deconvolution of XPS spectra of the Pd sample for (a) Bi 4f, (b) Pd 3d, (c) C 1s and (d) O 1s.

Table 10. Peak Properties of Bi 4f, Pd 3d, Pd 3p, C 1s, and O 1s Observed in the Pd Sample.

Spectrum	Position (eV)	Element	FWHM (eV)	Area	ASF	Corrected Area	Assignment
Bi 4f	157.1	Bi 4f7/2	0.87	716	7.4	97	Bi
Bi 4f	158.5	Bi 4f7/2	0.87	460	7.4	62	Bi <sub>l3-x</sub>
Bi 4f	159.2	Bi 4f7/2	0.87	152	7.4	21	Bi <sub>l3</sub>
Bi 4f	162.4	Bi 4f5/2	0.87	537	7.4	73	Bi
Bi 4f	163.8	Bi 4f5/2	0.87	345	7.4	47	Bi <sub>l3-x</sub>
Bi 4f	164.4	Bi 4f5/2	0.87	114	7.4	15	Bi <sub>l3</sub>
Pd 3d	335.0	Pd 3d5/2	1.03	4512	4.6	981	Pd
Pd 3d	336.5	Pd 3d5/2	1.03	6796	4.6	1477	Pd <sub>l2</sub>
Pd 3d	340.3	Pd 3d3/2	1.03	2978	4.6	647	Pd
Pd 3d	341.7	Pd 3d3/2	1.03	4486	4.6	975	Pd <sub>l2</sub>
C 1s	283.9	C 1s	1.38	871	0.25	3484	amorphous carbon
C 1s	285.6	C 1s	1.38	143	0.25	572	C bound to O
O 1s	533.1	Pd 3p3/2	3.69	5862	1.43	4099	Pd
O 1s	532.1	O 1s	1.80	378	0.66	573	O bound to C

In the Bi 4f7/2 region, three peaks are identified at 157.1, 158.5, and 159.2 eV, which are consistent with the literature values assigned to bismuth atoms in metallic bismuth,<sup>80</sup> Bi<sub>2</sub>O<sub>3</sub>,<sup>81</sup> and Bi<sub>l3</sub><sup>75</sup> respectively. However, the assignment of Bi<sub>2</sub>O<sub>3</sub> is not plausible as

the corresponding amount of oxygen is not observed in the O 1s spectrum. The peak at 158.5 eV is possibly due to bismuth atoms in a reduced iodine environment ( $\text{BiI}_{3-x}$  with  $x < 3$ ). The Pd 3d<sup>5/2</sup> peak deconvolutes into two peaks at 335.0 and 336.5 eV, which are assigned to palladium atoms in metallic palladium<sup>75</sup> and  $\text{PdI}_2^2$  respectively.

The C spectrum of the Pd sample has two peaks with the one at 283.9 eV assigned to amorphous carbon and the one at 285.6 eV assigned to carbon species bound to oxygen.<sup>75</sup> The O 1s spectrum is dominated by Pd 3p<sup>3/2</sup> peak at 533.1 eV.<sup>75</sup> The intensity of this peak (area under the peak) is consistent with the peak intensity in Pd 3d spectrum, which validates this peak assignment. The identification of oxygen peak in O 1s spectrum is difficult as the majority peak intensity is contributed by Pd atoms. The peak is fitted at 532.1 eV with a fixed 1:1 intensity ratio to the corresponding C 1s peak at 285.6 eV in C 1s spectrum.

XPS analysis indicates the existence of metallic Bi and  $\text{PdI}_2$  at the Pd-BiI<sub>3</sub> interface, which suggests that Pd reacts with BiI<sub>3</sub>. The majority of the bismuth elements on the surface exist in the form of metallic Bi (~54%) and BiI<sub>3-x</sub> (~35%), with a small portion (~11%) that remains as BiI<sub>3</sub>. The reactivity between Pd and iodine-rich crystals has been previously reported.<sup>82</sup> However, Pd is still widely used as the electrode contacts for iodide compound materials such as HgI<sub>2</sub> and PbI<sub>2</sub>.<sup>22,83-84</sup> There is no discussion on how this Palladium-iodine reactivity will affect the detector performance. This suggests that a careful re-evaluation of the electrode contacts for these materials is necessary.

#### 4.1.4.4 Pt Sample

Similar to the Pd sample, peak shifting is also observed in the Bi 4f spectrum in the Pt sample. The Pt 4f peaks exhibit an asymmetric feature, indicative multiple chemical states for the Pt atoms found in the interfacial region. However, this asymmetry is not due to reactivity therefore no attempt is made to deconvolve the peaks. The similar peak feature has been previously observed in Pt nanoparticles on pyrolytic graphite surfaces.<sup>85</sup> Since Pt was reported to have different electronic configurations for surface and bulk atoms,<sup>86</sup> the asymmetric peak was explained due to the surface Pt atoms in the 5d<sup>9</sup>6s<sup>1</sup> configuration, bulk Pt atoms in the 5d<sup>8</sup>6s<sup>2</sup> configuration, and surface Pt absorbed oxygen.<sup>85</sup> The peak properties and their assignments are summarized in Table 11.

Table 11. Peak properties of Bi 4f, Pd 3d, Pd 3p, C 1s, and O 1s observed in the Pt sample.

Spectrum	Position (eV)	Element	FWHM (eV)	Area	ASF	Corrected Area	Assignment
Bi 4f	157.1	Bi 4f7/2	0.86	2303	7.4	311	Bi
Bi 4f	158.3	Bi 4f7/2	0.86	1501	7.4	203	Bil <sub>3-x</sub>
Bi 4f	158.9	Bi 4f7/2	0.86	891	7.4	120	Bil <sub>3</sub>
Bi 4f	162.4	Bi 4f5/2	0.86	1727	7.4	233	Bi
Bi 4f	163.6	Bi 4f5/2	0.86	1125	7.4	152	Bil <sub>3-x</sub>
Bi 4f	164.2	Bi 4f5/2	0.86	669	7.4	90	Bil <sub>3</sub>
I 3d	618.6	I 3d5/2	1.12	10385	6	1731	Bil <sub>3</sub>
I 3d	619.4	I 3d5/2	1.12	4365	6	728	I <sub>2</sub>
I 3d	630.1	I 3d3/2	1.12	7555	N/A		Bil <sub>3</sub>
I 3d	630.9	I 3d3/2	1.12	2550	N/A		I <sub>2</sub>
C 1s	284.0	C 1s	1.46	884	0.25	3536	amorphous carbon
C 1s	285.9	C 1s	1.46	259	0.25	1036	C bound to O
O 1s	529.5	O 1s	1.59	185	0.66	280	O bound to Pt
O 1s	532.0	O 1s	1.59	624	0.66	945	O bound to C

The assignment for Bi 4f spectrum is similar to that in Pd sample. The Bi 4f<sup>7/2</sup> peaks at 157.1, 158.3, and 158.9 eV are assigned to bismuth atoms in metallic bismuth, Bil<sub>3-x</sub>, and Bil<sub>3</sub> respectively. The existence of I<sub>2</sub> is evidenced by the peak at 619.4 eV in I 3d spectrum.<sup>75</sup> The two peaks in C 1s spectrum are assigned to amorphous carbon at 284.0 eV and carbon species bound to oxygen at 285.9 eV. The O 1s spectrum deconvolves into two peaks with the one at 529.5 eV assigned to oxygen bound to Pt and the one at 532.0 eV assigned to oxygen bound to carbon. The uphill tail in the low energy side of O 1s spectrum is the trail of Pt 4p<sup>3/2</sup> peak at 520 eV.<sup>75</sup>

The XPS results indicate that Pt is not good as the contact material for Bil<sub>3</sub> either. The effect of Pt on the surface of Bil<sub>3</sub> is different from that of Pd. Here the presence of Pt causes the reduction of Bil<sub>3</sub>. But unlike Pd, Pt is not involved in the reaction. The function of Pt in this case is similar to that of a catalyst.

#### 4.1.5 AFM Analysis

AFM characterization has been used to check the distribution of the sputtered metals on the surface of Bil<sub>3</sub> (Figure 31). It is observed that Au fully covers the Bil<sub>3</sub> surface while Pd and Pt form islands, which indicates a completely wetting of Au on the Bil<sub>3</sub> surface while non-wetting characteristic of Pd and Pt. The islands on the Pt sample surface are more sparsely distributed with higher height compared to the Pd sample. To verify if the islands are formed by the deposited metals or by other species produced in the metal-Bil<sub>3</sub> interaction, the volume of the islands is calculated using an image processing software (Scanning Probe Image Processing, SPIPTM) by analyzing the scanned

histogram of the surface. The calculated island volume for Pd sample is  $4.6 \times 10^6 \text{ nm}^3$  on a  $4 \mu\text{m}^2$  area, which is corresponding to a thickness of 1.15 nm if the Pd island volumes were evenly spread on the surface. This matches well with the experimentally deposited thickness of 1 nm and suggests that the islands are mainly formed by Pd. The island volume on Pt sample is calculated to be  $7.7 \times 10^8 \text{ nm}^3$  on a  $100 \mu\text{m}^2$  area, which is corresponding to a deposited thickness of 7.7 nm. This result has a large deviation from the experiment (1 nm), which suggests that species generated by the reaction, i.e.  $\text{I}_2$ , may deposit on the surface.

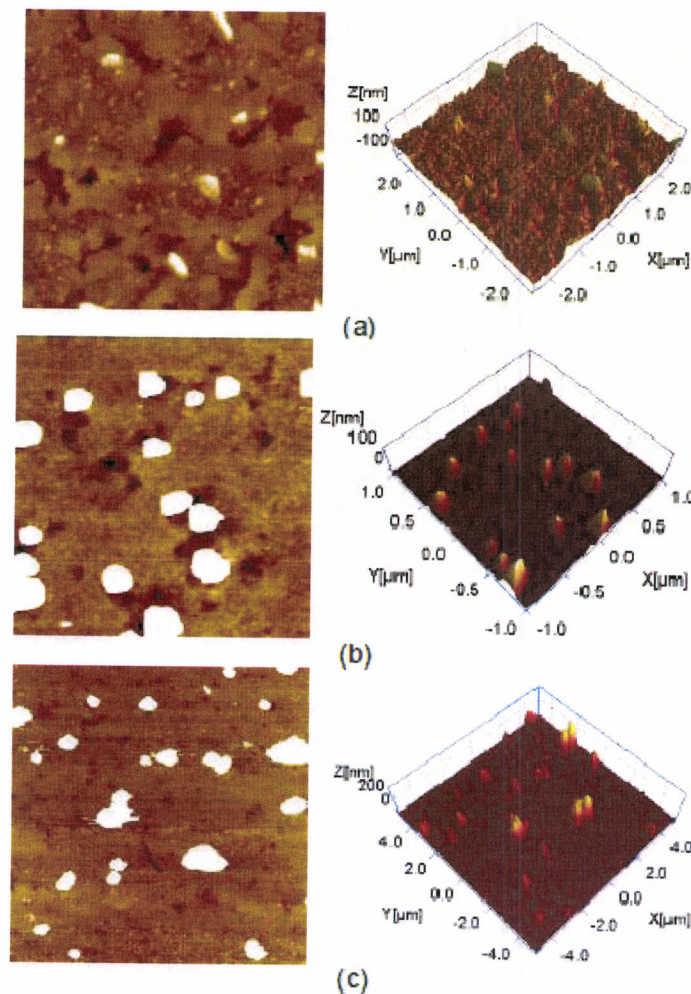


Figure 31. AFM image and 3D view of topography for the (a) Au sample, (b) Pd sample, and (c) Pt sample.

#### 4.1.6 I-V Characterization

The resistivity of  $\text{BiI}_3$  single crystals has been measured with Au, Pd, and Pt electrodes. The crystal samples were cut from adjacent positions of a large single crystal to minimize the sample variation. The I-V curves for crystals with different electrodes are

shown in Figure 32. It is observed that the crystal with Au electrodes has the highest resistivity, and the one with Pd electrodes shows the lowest, as summarized in Table 12.

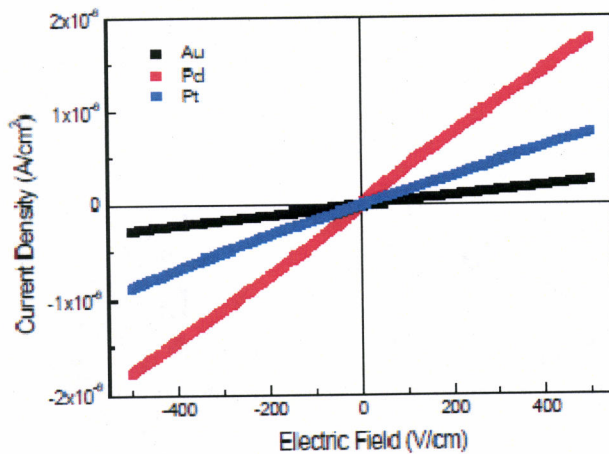


Figure 32. Typical I-V characteristic curves for  $\text{BiI}_3$ .

Table 12. Sample Information and Resistivity of  $\text{BiI}_3$  Single Crystals for I-V Characterization

Sample #	Electrode	Surface Area (cm <sup>2</sup> )	Thickness (cm)	Resistivity 10 <sup>9</sup> ( $\Omega\cdot\text{cm}$ )
1	Au	0.260	0.075	1.85
2	Pd	0.167	0.075	0.28
3	Pt	0.251	0.076	0.61

The similar results were also reported by Fornaro *et al.* on  $\text{BiI}_3$  crystals grown by PVT method.<sup>3</sup> Given that  $\text{Bi}^{3+}$  ions are reduced to metallic Bi at the Pd- $\text{BiI}_3$  interface, the Bi atoms could drift across the crystal body under an external electric field. This will decrease the effective thickness between the electrodes. Consequently, the measured resistivity is smaller than the actual value.

Based on the XPS results, Au is expected to be physically contacted with  $\text{BiI}_3$ , the measured resistivity thus represents a more accurate value of this material. The sample with Pt electrodes shows resistivity in between, which is possibly due to the drift of  $\text{Bi}^{3+}$  ions resulting from less binding of iodine.

#### 4.2 Radiation Sensing

We cut  $\text{BiI}_3$  crystals using a diamond wire saw purchased for this project from MTI Corporation. This wire saw has variable pressure and saw rotation speed which allows us to investigate for cutting and surface damage due to the detector fabrication process. An example of one of our first cut detector crystals is shown in Figure 33. Detectors of various with Pd electrodes were fabricated for testing.

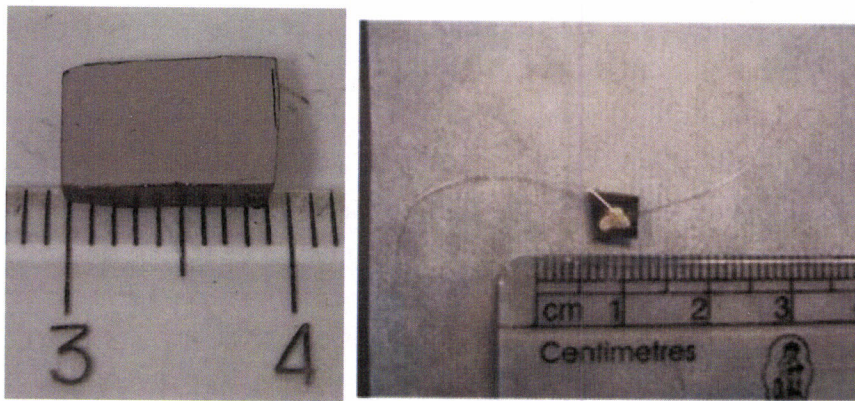


Figure 33. Left: Cut  $\text{BiI}_3$  crystal prepared for electrode (Pd) deposition. Right: Fabricated detector after electrode deposition and wire bonding.

To prepare for testing, we built two test boxes for the detectors. We measured signals from the anode and cathode electrodes. Amptek A250 charge sensitive preamplifiers were installed into a light-tight aluminum box. We also developed a data acquisition system to be used in detector testing. This program, built using LabView, has the capability to digitize the preamplifier signals and perform acquire both spectral and timing information from the detectors. A screen shot of the data acquisition interface is shown in Figure 34. The system was tested with  $\text{LaBr}_3$  crystals in our laboratory. Unfortunately, the sampling speed of the data acquisition card is 1 MHz per channel for 4 channels. This sampling speed may not be able to accurately measure from the preamplifier. Data from shaping amplifiers showed much improved energy accuracy and improved energy resolution. Thus, we modified the program to accept both signals from the preamplifier and shaping amplifier to ensure that we can collect all information from the detector.

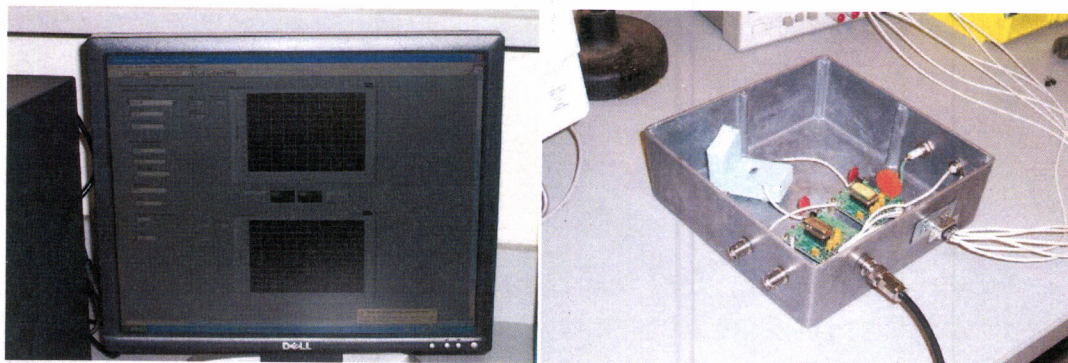


Figure 34. Screenshot showing front display for LabView data acquisition program to collect spectral and timing information from detectors (Left). Test box with preamplifiers and detector (Right).

#### 4.2.1 Measurement of Electron Mobility

The mobility of electrons and holes is one property that helps describe the charge transport characteristics in a semiconductor detector. A detector with high and uniform charge carrier properties throughout the material will generally perform better as a radiation detector and spectrometer. In planar detectors with ohmic contacts, the electric field should be relatively uniform. The mobility ( $\mu$ ) of electrons and holes can be estimated by measuring the drift time ( $t_{drift}$ ) from an interaction in a detector. To estimate the mobility of electrons, one can use alpha particles that will be stopped in a few  $\mu\text{m}$ , irradiated from the cathode side of the detector, forcing electrons to drift the entire thickness (D) of the detector. In this case, the mobility of electrons can be calculated by

$$\mu_e = \frac{D}{Et_{drift,e}} \quad (15)$$

where E is the strength of the electric field (V/cm), and the subscript e represents electrons. We collected a pulse waveform from a  $\text{BiI}_3$  detector (Figure 35). By measuring the rise time of the signal, we get the drift time of the electrons.

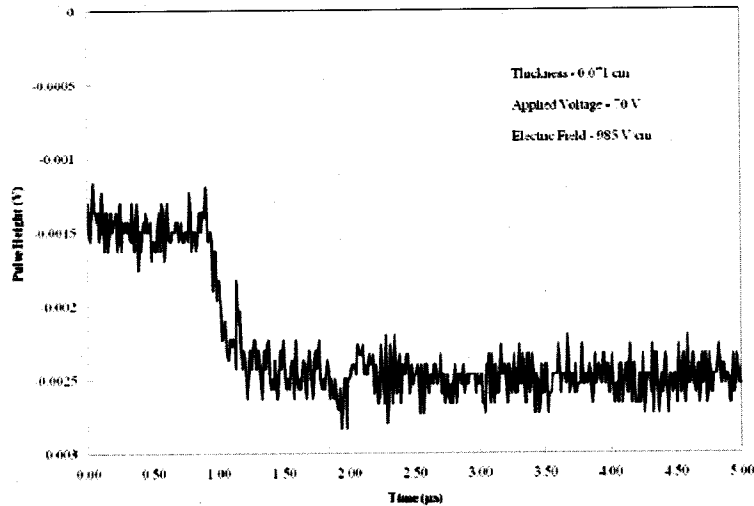


Figure 35. Pulse waveform from an Am-241 alpha-particle irradiated from the cathode. By measuring the drift time of the electrons creating the signal, a mobility for electrons can be estimated.

The drift time for the electrons in the above waveform was estimated to be approximately 250 ns (0.25  $\mu\text{s}$ ). Thus, using the detector thickness of 0.071 cm and the applied voltage of 70 V, we estimate the mobility of electrons in this detector to be approximately  $250 \pm 50 \text{ cm}^2/\text{V}\cdot\text{s}$ . The uncertainty in this value is based on several factors, including the range of alpha particles in  $\text{BiI}_3$ , contributions from electronic noise, and uncertainty in drift time. It should also be noted that this value is approximately a factor of 2 less than previously reported values for  $\text{BiI}_3$  electron mobility. We are

currently investigating reasons for the discrepancy. It should also be noted that the signal strength of only  $\sim 1$  mV was much lower than expected. We estimated that the signal amplitude should have been about 40 mV. Possible reasons for the poor signal (and additional uncertainty in mobility) include dead layer formation near the electrodes where alpha particle would be stopped, and poor electrode contacts where the signal size would be reduced due to weighting potential effects.

#### 4.2.2 X-Ray/Gamma-Ray Detection

The detectors were tested with a low-current (0.1 mA) 60 kVp x-ray source. The detectors were connected to an Amptek A250 preamplifier and were connected to standard Ortec NIM electronics. An example spectra is shown on the right in Figure 36. Signals from the preamp (analyzed on an oscilloscope) were almost an order of magnitude lower than expected (< 0.5 mV instead of 8-10 mV). This small signal suggests that improvements in surface preparation may be necessary in order to increase the signal from the detector.

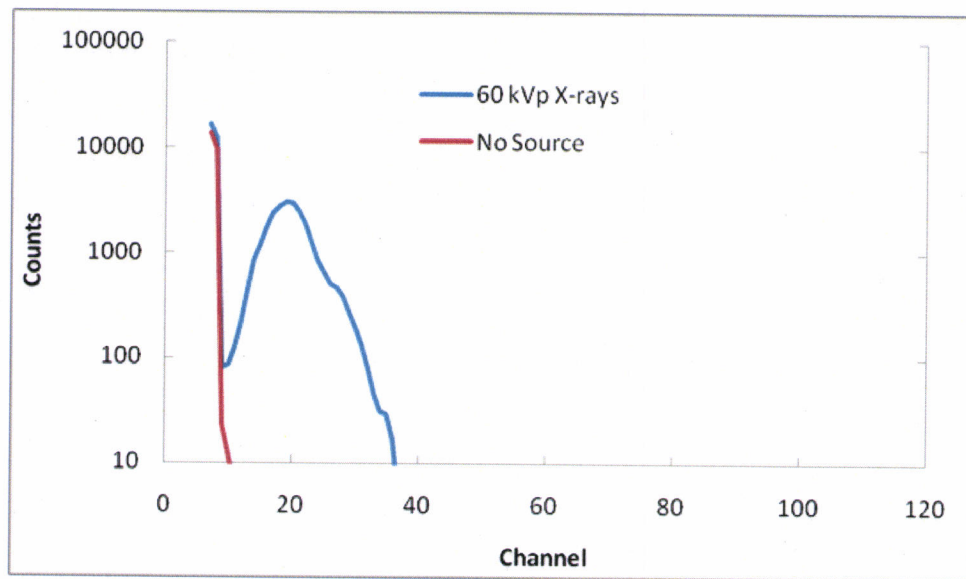


Figure 36. 60 kVp X-ray spectra. A  $1 \text{ cm}^2$  collimated beam was irradiated on the cathode side of the detector. (-50 V bias, 1  $\mu\text{s}$  shaping time).

## 5. Conclusions

The increasing demand for room temperature gamma-ray detectors encourages the discovery and development of high quality compound semiconductor materials. The required material properties include high density and atomic numbers for high gamma-ray detection efficiency; moderate bandgap between 1.5 eV and 3 eV for room temperature operation and generation of large number of electron-hole pairs, and high resistivity for improved signal to noise ratio.  $\text{BiI}_3$  meets all these criteria thus has the potential to be a successful material for room temperature gamma-ray detection applications.

Crystal growth is the most challenging and time-consuming stage of developing a new detector material. This work presented the efforts of growing large volume  $\text{BiI}_3$  single crystals using MVB method. The whole growth process is composed of different stages including heating up from room temperature to the maximum process temperature, soaking for a period of time, cooling down to growth temperature, crystal growth, and post-growth cooling down to room temperature. Each stage has been carefully designed and tested to ensure the smooth growth run. The crystal growth was conducted at a total of nine growth conditions (variation of growth rate and temperature gradient at solid-liquid interface), among which only three conditions produced single crystals. The phase purity of the grown single crystals was verified by XRD. The quality of the single crystals was characterized by EPD measurement and X-ray rocking curve  $\omega$ -scans. For EPD measurement, the etching recipe was determined to be 10 sec immersion in 15% KI solution. The observed EPD values for all the crystals were on the order of magnitude of  $\sim 10^4 \text{ cm}^{-2}$ , which was comparable to other compound semiconductor crystals such as  $\text{HgI}_2$  and lab produced CZT, but one order of magnitude higher than the commercial CZT crystals. The high EPD values indicated the high dislocation densities in the crystals. Among the crystals grown by MVB method, the one grown at  $10^\circ\text{C}/\text{cm}$  and 0.5 mm/h showed the smallest average EPD values. The rocking curve  $\omega$ -scan peaks for all the crystals showed similar FWHM and peak characteristics. Peak broadening with multiple peaks and shoulders were observed. The poor crystalline perfection was commonly observed among the iodide compound crystals such as  $\text{HgI}_2$  and  $\text{PbI}_2$ , which implied that the imperfections were possibly caused by the residual strains induced during the cooling of the crystals due to the softness of these materials. In addition, the deformation during handling and cutting could also contribute to the broadening of the rocking curves. Although the  $\text{BiI}_3$  single crystals grown at three different conditions did not show distinct differences of EPD values and rocking curve characteristics, the crystals grown at  $10^\circ\text{C}/\text{cm}$  and 0.5 mm/h were selected for further studies due to their slightly better qualities. A single crystal with a dimension of  $18 \times 13 \times 5 \text{ mm}^3$ , the largest crystal size ever reported for  $\text{BiI}_3$ , was obtained at this growth condition.

The cleaved surface of  $\text{BiI}_3$  was characterized by SEM and AFM respectively. The SEM characterization indicated a crack-free and macroscopically smooth surface. The AFM topographic image revealed an atomically rough (001) surface with average roughness of 0.486 nm. The irregular edges of the atomic layers were attributed to the weak van

der waal's forces between the layers. The chemical composition at the surface of  $\text{BiI}_3$  was characterized to be of  $\text{BiI}_{2.78}$  by XPS. The iodine deficiency was attributed to the dissociation of  $\text{BiI}_3$  into Bi and  $\text{I}_2$  during cooling of the crystal, and the evaporation of iodine when exposed in air. The surface oxidation was also observed for  $\text{BiI}_3$  crystals exposed in air for over two weeks, which suggested that a proper sealing or inert gas environment is necessary for the crystal storage.

Through UV-Vis transmission and reflection spectra, the band gap of  $\text{BiI}_3$  was characterized to be of  $1.68 \pm 0.09$  eV with indirect transition characteristic. The band gap value of  $\text{BiI}_3$  was observed to decrease with increasing temperature, which is commonly observed in semiconductor materials. The impurity concentrations in commercial powder and  $\text{BiI}_3$  crystals were observed to be as high as  $10^{17} \text{ cm}^{-3}$ , at which the band gap narrowing effect was likely to happen. The band gap value determined in this work was consistent with previous studies using UV-Vis spectra. The indirect band transition was confirmed by the most recent theoretical calculation on the band structure of  $\text{BiI}_3$  using DFT. The large difference between the band gaps determined by UV-Vis spectra and ellipsometry was attributed to the different absorption coefficient  $\alpha$  used to extract the band gap. For  $\text{BiI}_3$ , band gap determined by UV-Vis spectra was more accurate.

Through the characterizations on  $\text{BiI}_3$  single crystals grown in this work, it was found that the crystals have high impurity concentrations and dislocation densities. The crystal quality is not comparable to the commercial CdTe and CZT crystals. While the material was observed to be sensitive to radiation (alphas, gamma-rays, and x-rays), the current material was not stable and would severely polarize, which may be attributable to the high impurity concentrations and motion of impurities at high voltage. The future work should focus on resolving these problems, improving the purity of the material, and developing  $\text{BiI}_3$  towards a room temperature gamma-ray spectrometer.

## **6. Additional Information**

### **6.1 Papers and Presentations Created in Whole or in Part by This Funding**

The following papers and presentations were made possible by the funding received by this project (in whole or in part). In addition to the listed publications, at least one additional paper and Ph.D. thesis associated with this project should be completed in the future.

#### **6.1.1 Publications**

- A. T. Lintereur, W. Qiu, J. C. Nino, and J. E. Baciak, "Characterization of Bismuth Tri-Iodide Single Crystals for Wide Band-Gap Semiconductor Radiation Detectors," accepted in *Nuclear Instruments and Methods in Physics Research Part A*, 2011.
- Qiu, Wei, "Growth and Characterization of Bismuth Tri-Iodide Single Crystals by Modified Vertical Bridgman Method," Ph.D. Thesis, University of Florida, 2010.
- W. Qiu, A. T. Lintereur, J. C. Nino, and J. E. Baciak, "Growth and Characterization of  $\text{BiI}_3$  Single Crystals for Room Temperature Gamma-Ray Detection Grown by Modified Bridgman Method," submitted to *Journal of Crystal Growth*, 2009.
- A. T. Lintereur, W. Qiu, J. C. Nino, and J. E. Baciak, "Growth and Characterization of  $\text{BiI}_3$  Single Crystals for Room Temperature Gamma-Ray Detection Grown by Modified Bridgman Method," *Hard X-Ray, Gamma-Ray and Neutron Detectors Physics, Proceedings of SPIE<sup>2</sup>*, Vol. 7449, pp. 744958 1-8, 2009.
- A. T. Lintereur, W. Qiu, J. C. Nino, and J. E. Baciak, "Iodine Based Compound Semiconductors for Room Temperature Gamma-Ray Spectroscopy," *Optics and Photonics in Global Homeland Security IV, Proceedings of SPIE<sup>2</sup>*, Volume 6945, pp. 694503 1-9, 2008.

#### **6.1.2 Presentations**

- A. T. Lintereur, W. Qiu, J. C. Nino, and J. E. Baciak, "Electrical Characterization of Bismuth Iodide Crystals," 2010 IEEE Nuclear Science Symposium and Medical Imaging Conference, Knoxville, TN, November 1-6, 2010.
- A. T. Lintereur, W. Qiu, J. C. Nino, and J. E. Baciak, "Characterization of  $\text{BiI}_3$  Single Crystals for Wide Band-Gap Semiconductor Radiation Detectors," 2010 Symposium on Radiation Measurements and Applications (SORMA), Ann Arbor, MI, May 24-28, 2010.
- J. E. Baciak, J. C. Nino, W. Qiu, and A. T. Lintereur, "Single Crystal Bismuth Iodide ( $\text{BiI}_3$ ) Radiation Detectors," 2010 ANS Radiation Protection and Shielding Division Topical Meeting, Las Vegas, NV, April 18-23, 2010.

- J. E. Baciak, "High Z, Wide Bandgap Semiconductor Materials for Radiation Detection," 2010 ANS Student Conference, Ypsilanti, MI, April 8-11, 2010.
- A. T. Lintereur, W. Qiu, J. C. Nino, and J. E. Baciak, "Characterization of  $\text{BiI}_3$  Single Crystals Grown by Modified Bridgman Method," 2009 IEEE Nuclear Science Symposium and Medical Imaging Conference, Orlando, FL, October 25-31, 2009.
- A. T. Lintereur, W. Qiu, J. C. Nino, and J. E. Baciak, "Growth and Characterization of  $\text{BiI}_3$  Single Crystals for Room Temperature Gamma-Ray Detection Grown by Modified Bridgman Method," presented at 2009 SPIE Optics and Photonics Conference, San Diego, CA, August 2-7, 2009.
- W. Qiu, A. T. Lintereur, H. Xu, S. R. Phillipot, J. E. Baciak, and J. C. Nino, "Crystal Growth and Characterization of Bismuth Tri-Iodide by Modified Bridgman Method," 2009 Materials Research Society Spring Meeting, San Francisco, CA, April 13-17, 2009.
- W. Qiu, A. T. Lintereur, J. C. Nino, and J. E. Baciak, "Growth and Characterization of Single Crystal  $\text{BiI}_3$ ," presented at 2009 ANS Student Conference, Gainesville, FL April 2-4, 2009.
- Azaree T. Lintereur, Wei Qiu, Juan C. Nino, and James E. Baciak, "Bismuth Tri-Iodide for Room Temperature Gamma-Ray Spectroscopy," 2008 IEEE Nuclear Science Symposium and Medical Imaging Conference, Dresden, GERMANY, October 19-25, 2008.
- Wei Qiu, Azaree T. Lintereur, James E. Baciak, and Juan C. Nino, "Bismuth Iodide Single Crystals for Gamma-Ray Detection", Sensors and Actuators Symposium F, Electroceramics XI conference, Manchester, UNITED KINGDOM, September 1st, 2008.
- W. Qiu, A. T. Lintereur, J. C. Nino, and J. E. Baciak, "Growth and Characterization of Bismuth Iodide Crystals Growth by the Bridgman Method," 2008 SPIE Defense and Security Conference, Orlando, FL March 17-20, 2008.
- A. T. Lintereur, W. Qiu, J. C. Nino, and J. E. Baciak, "Iodine Based Compound Semiconductors for Room Temperature Gamma-Ray Spectroscopy," 2008 SPIE Defense and Security Conference, Orlando, FL March 17-20, 2008.
- J. E. Baciak, "Iodine Based Compound Semiconductor Radiation Detectors," 2008 ANS Student Conference, College Station, TX, February 28-March 1, 2008.

## 6.2 Transitions and Future Funding

In 2007, we proposed related research to the Department of Energy's NNSA FY08 PDP BAA to investigate electrode-surface interfaces for  $\text{BiI}_3$  and the potential utilization of coplanar grid and pixelated electrodes. In April 2009, this proposal was selected for

funding. The funding began on approximately October 1, 2009 and will fund the  $\text{BiL}_3$  project for three years, beyond the DTRA funding ending on May 15, 2010.

## References

1. Y.N. Dmitriev, P.R. Bennett, L.J. Cirignano, M. Klugerman, and K.S. Shah, "Bismuth Iodide Crystals as a Detector Material: Some Optical and Electrical Properties," *Proc. SPIE-Int. Soc. Opt. Eng.*, **3768** 521-529 (1999).
2. M. Matsumoto, K. Hitomi, T. Shoji, and Y. Hiratake, "Bismuth Tri-iodide Crystal for Nuclear Radiation Detectors," *IEEE Trans. Nucl. Sci.*, **49** [5] 2517-2520 (2002).
3. L. Fornaro, A. Cuna, A. Noguera, M. Perez, and L. Mussio, "Growth of Bismuth Tri-iodine Platelets for Room Temperature X-ray Detection," *IEEE Trans. Nucl. Sci.*, **51** [5] 2461-2465 (2004).
4. L. Fornaro, I. Aguiar, A. Noguer, M. Perez, and M. Rodriguez, "Improvements on Bismuth Tri-iodide Platelets For Room Temperature X-ray Detection," *IEEE Nuclear Science Symposium, R04-3* [2] 3616-3621 (2006).
5. P.W. Bridgman, "Certain Physical Properties of Single Crystals of Tungsten, Antimony, Bismuth, Tellurium, Cadmium, Zinc, and Tin..," *Proc. Am. Aca. Arts Sci.*, **60** [1/14] 305-383 (1925).
6. J.C. Brice, "Crystal Growth Processes", p. 150, Blackie & Son Ltd., Glasgow and London, 1986.
7. F.M. Carlson, A.L. Fripp, and R.K. Crouch, "Thermal-Convection during Bridgman Crystal-Growth," *J. Cryst. Growth*, **68** [3] 747-756 (1984).
8. M.C. Flemings, "Solidification Processing", McGraw-Hill, Inc., New York, 1974.
9. P.C. Sukanek, "Deviation of Freezing Rate from Translation Rate in the Bridgman-Stockbarger Technique .1. Very Low Translation Rates," *J. Cryst. Growth*, **58** [1] 208-218 (1982).
10. P.C. Sukanek, "Deviation of Freezing Rate from Translation Rate in the Bridgman-Stockbarger Technique .2. Moderate Translation Rates," *J. Cryst. Growth*, **58** [1] 219-228 (1982).
11. P. Rudolph, F. Matsumoto, and T. Fukuda, "Studies on Interface Curvature during Vertical Bridgman Growth of InP in a Flat-bottom Container," *J. Cryst. Growth*, **158** [1-2] 43-48 (1996).
12. L.Y. Chin and F.M. Carlson, "Finite-Element Analysis of the Control of Interface Shape in Bridgman Crystal-Growth," *J. Cryst. Growth*, **62** [3] 561-567 (1983).
13. S.H. Hahn and J.K. Yoon, "Numerical Analysis for the Application of Radiative Reflectors to Vertical Bridgman Growth Configurations," *J. Cryst. Growth*, **177** [3-4] 296-302 (1997).
14. S. Kuppurao and J.J. Derby, "Designing Thermal Environments to Promote Convex Interface Shapes during the Vertical Bridgman Growth of Cadmium Zinc Telluride," *J. Cryst. Growth*, **172** [3-4] 350-360 (1997).
15. O.Y. Hong and S.Y. Wei, "Numerical simulation of CdTe vertical Bridgman growth," *J. Cryst. Growth*, **173** [3-4] 352-366 (1997).

16. A. Bachran, P. Reinshaus, and W. Seifert, "Influence of Thermal Processing Parameters and Material Properties on Velocity Configurations in Semiconductor Melts during the Vertical Bridgman Growth Technique," *Cryst. Res. Technol.*, **33** [1] 27-36 (1998).
17. V.M. Lakeenkov, V.B. Ufimtsev, N.I. Shmatov, and Y.F. Schelkin, "Numeric simulation of vertical Bridgman growth of Cd<sub>1-x</sub>Zn<sub>x</sub>Te melts," *J. Cryst. Growth*, **197** [3] 443-448 (1999).
18. H.J. Lee and A.J. Pearlstein, "Simulation of radial solute segregation in vertical Bridgman growth of pyridine-doped benzene, a surrogate for binary organic nonlinear optical materials," *J. Cryst. Growth*, **218** [2-4] 334-352 (2000).
19. F. Rosenberger, "Crystal Growth in Science and Technology", *NATO ASI Series*, Edited by H. Arend and J. Hulliger, Plenum Press, New York, 1989.
20. P. Capper, "Bulk Crystal Growth of Electronic, Optical & Optoelectronic Materials", *Materials for Electronic and Optoelectronic Applications*, Edited by P. Capper, S. Kasap, and A. Willoughby, John Wiley & Sons, Ltd, West Sussex, England, 2005.
21. A. Cuna, A. Noguera, E. Saucedo, and L. Fornaro, "Growth of Bismuth Tri-iodide Platelets by the Physical Vapor Deposition Method," *Cryst. Res. Technol.*, **39** [10] 912-919 (2004).
22. L. Fornaro, E. Saucedo, L. Mussio, A. Gancharov, and A. Cuna, "Bismuth Tri-iodide Polycrystalline Films for Digital X-ray Radiography Applications," *IEEE Trans. Nucl. Sci.*, **51** [1] 96-100 (2004).
23. R. Cadoret, "Alpha-Mercuric Iodide Crystal-Growth by Physical Vapor Transport," *J. Cryst. Growth*, **146** [1-4] 9-14 (1995).
24. I. Sunagawa, "Crystals: Growth, Morphology, and Perfection", Cambridge University Press, Cambridge, UK, 2005.
25. D. Cubicciotti and F.J. Keneshea, "The Vapor Pressures of BiI<sub>3</sub> over Liquid Bi-BiI<sub>3</sub> Solutions," *J. Phys. Chem.*, **63** [2] 295-297 (1959).
26. M. Ohyama, "Thermal Instability of Growth Interface in Horizontal Solidification of GaAs," *J. Phys. Soc. Jpn.*, **29** [3] 706-710 (1970).
27. E. Kuroda, H. Kozuka, and Y. Takano, "The Effect of Temperature Oscillations at the Growth Interface on Crystal Perfection," *J. Cryst. Growth*, **68** [2] 613-623 (1984).
28. Y. Wang, K. Kudo, Y. Inatomi, R.B. Ji, and T. Motegi, "Growth Interface of CdZnTe Grown from Te Solution with THM Technique under Static Magnetic Field," *J. Cryst. Growth*, **284** [3-4] 406-411 (2005).
29. D. Nason and L. Keller, "The Growth and Crystallography of Bismuth Tri-Iodide Crystals Grown by Vapor Transport," *J. Cryst. Growth*, **156** [3] 221-226 (1995).

30. S.V. Tsivinskii and L.A. Maslova, "Rocking Curve Half-Width Obtained by Means of a Double X-Ray Crystal Spectrometer and Dislocation Density in Single-Crystals," *Mater Sci Eng*, **30** [2] 147-153 (1977).
31. C.R. Wie, "Relaxation and Rocking-Curve Broadening of Strained (Ga,In) as Single Layers on (001) GaAs," *J. Appl. Phys.*, **65** [6] 2267-2271 (1989).
32. S. Nam, Y.M. Yu, J. Rhee, B. O, Y.D. Choi, J. Lee, and Y.J. Jung, "Evaluation of Crystal quality of ZnTe/GaAs Epilayers by the Double Crystal Rocking Curve," *Mater. Chem. Phys.*, **69** [1-3] 30-35 (2001).
33. J.G. Wood and R.S. Marriner, "The Measurement of Vickers Hardness Indentations," *Metallurgia*, **73** [440] 297-300 (1966).
34. K. Baskar, K. Thangaraj, and R. Gobinathan, "Hardness Anisotropy of Mercuric Iodide Single-Crystals," *J. Mater. Sci. Lett.*, **10** [2] 85-86 (1991).
35. W.F. Gale and T.C. Totemeier, "Smithells Metals Reference Book", 8th Edition, Elsevier Butterworth-Heinemann, New York, 2004.
36. E. Springer, "Relation between Dislocation Density and Etch Pit Density in Germanium," *Z. Metallkd.*, **62** [4] 298-300 (1971).
37. D.J. Stirlan, G.J. Rees, and A. Ritson, "The Relationship between Etch Pit Density and Dislocation Density for (001)GaAs," *J. Cryst. Growth*, **79** [1-3] 493-502 (1986).
38. R. Hirano, "Growth of Low Etch Pit Density Homogeneous 2" InP Crystals Using a Newly Developed Thermal Baffle," *Jpn. J. Appl. Phys., Part 1*, **38** [2B] 969-971 (1999).
39. D. Hull and D.J. Bacon, "Introduction to Dislocations", 3rd Edition, Pergamon Press, New York, 1984.
40. D.S. McGregor and H. Hermon, "Room-temperature Compound Semiconductor Radiation Detectors," *Nucl. Instrum. Methods Phys. Res., Sect. A*, **395** [1] 101-124 (1997).
41. J.P. Ponpon, R. Stuck, P. Siffert, B. Meyer, and C. Schwab, "Properties of Vapor-Phase Grown Mercuric Iodide Single-Crystal Detectors," *IEEE Trans. Nucl. Sci., Ns22* [1] 182-191 (1975).
42. P.T. Randtke and C. Ortale, "Effects of Dislocations and Crystal Defects on Energy Resolution and Response Uniformity of Mercuric Iodide Detectors," *IEEE Trans. Nucl. Sci.*, **24** [1] 129-134 (1977).
43. L. Fornaro, L. Luchini, M. Koncke, L. Mussio, E. Quagliata, K. Chattopadhyay, and A. Burger, "Growth of Mercuric Iodide Platelets for X-ray Room Temperature Detectors in the HgI<sub>2</sub>-HI-H<sub>2</sub>O system," *J. Cryst. Growth*, **217** [3] 263-270 (2000).
44. T.E. Schlesinger, J.E. Toney, H. Yoon, E.Y. Lee, B.A. Brunett, L. Franks, and R.B. James, "Cadmium Zinc Telluride and Its Use as a Nuclear Radiation Detector Material," *Mater. Sci. Eng., R*, **32** [4-5] 103-189 (2001).

45. P. Cheuvart, U. Elhanani, D. Schneider, and R. Triboulet, "CdTe and CdZnTe Crystal-Growth by Horizontal Bridgman Technique," *J. Cryst. Growth*, **101** [1-4] 270-274 (1990).
46. M. Schieber, R.B. James, J.C. Lund, D.S. McGregor, T.S. Gilbert, J.M. VanScyoc, R.W. Olsen, A.E. Pontau, T.S. Schlesinger, and J. Toney, "State of the art of wide-bandgap semiconductor nuclear radiation detectors," *Nuovo Cimento A*, **109** [9] 1253-1260 (1996).
47. J.M. Tartaglia, S.M. Crochiere, C.E. Kalnas, D.L. Farrington, J.A. Kronwasser, and P.J. Pearah, "A Study of Etch Pit Density and X-Ray Rocking Curves for GaAs Substrate Evaluation," *J. Electron. Mater.*, **20** [5] 345-352 (1991).
48. H. Yoon, C. Yoon, C.S. Park, T. Ko, N.S. Kim, and K.N. Han, "Quantitative Determination of PGM using ICP-MS, ICP-AES, AAS and XRF," *Miner. Metall. Process.*, **22** [1] 59-64 (2005).
49. Rashmi, U. Dhawan, and D.K. Suri, "Evaluation of uncertainty of measurement in quantitative XRF analysis: I. Scattered radiation method," *X-Ray Spectrom.*, **28** [3] 157-162 (1999).
50. Z.H. Li, W.T. Li, J. Liu, B.J. Zhao, S.F. Zhu, H.P. Xu, and H. Yuan, "Improved Technique for HgI<sub>2</sub> Purification," *J. Cryst. Growth*, **156** [1-2] 86-90 (1995).
51. J.F. Condeles, R.C.Z. Lofrano, J.M. Rosolen, and M. Mulato, "Stoichiometry, Surface and Structural Characterization of Lead Iodide Thin Films," *Braz J Phys*, **36** [2A] 320-323 (2006).
52. V.B. Timofeev and V.I. Vashchen, "Optical Properties of BiI<sub>3</sub> Single Crystals near Long-Wavelength Edge of Fundamental Absorption," *Opt. Spectrosc.*, **24** [5] 396 (1968).
53. Vashchen.Vi and V.B. Timofeev, "Absorption Spectra and Indirect Optical Transitions in BiI<sub>3</sub> Single Crystals," *Soviet Physics Solid State, Ussr*, **9** [6] 1242-& (1967).
54. G.E. Jellison, J.O. Ramey, and A.A. Boatner, "Optical Functions of BiI<sub>3</sub> as Measured by Generalized Ellipsometry," *Phys. Rev. B*, **59** [15] 9718-9721 (1999).
55. M. Schluter, M.L. Cohen, S.E. Kohn, and C.Y. Fong, "Electronic-Structure of BiI<sub>3</sub>," *Phys. Status Solidi B*, **78** [2] 737-747 (1976).
56. P.J. Dean and D.G. Thomas, "Intrinsic Absorption-Edge Spectrum of Gallium Phosphide," *Physical Review*, **150** [2] 690-703 (1966).
57. J.I. Pankove, "Optical Processes in Semiconductors", Prentice-Hall, Englewood Cliffs, 1971.
58. B.J. Curtis and H.R. Brunner, "Crystal-Growth of Bismuth Iodide," *Mater. Res. Bull.*, **9** [5] 715-720 (1974).
59. T. Komatsu, T. Karasawa, T. Iida, K. Miyata, and Y. Kaifu, "Secondary-Emission of Indirect Exciton in BiI<sub>3</sub>," *J. Lumin.*, **24-5** [Nov] 679-682 (1981).

60. H. Yorikawa and S. Muramatsu, "Theoretical study of crystal and electronic structures of  $\text{BiI}_3$ ," *Journal of Physics-Condensed Matter*, **20** [32] - (2008).
61. Y. Kaifu and T. Komatsu, "Optical-Properties of Bismuth Tri-Iodide Single-Crystals .2. Intrinsic Absorption-Edge," *J. Phys. Soc. Jpn.*, **40** [5] 1377-1382 (1976).
62. W.W. Piper, P.D. Johnson, and D.T.F. Marple, "Temperature Dependence of the Optical Band Gap in ZnS," *J. Phys. Chem. Solids*, **8** 457-461 (1959).
63. G.D. Mahan, "Temperature Dependence of Band Gap in CdTe," *Journal of Physics and Chemistry of Solids*, **26** [4] 751-& (1965).
64. A.G. Dmitriev, "Temperature-Dependence of the Width of the GaAs Band-Gap," *Semiconductors*, **29** [3] 227-229 (1995).
65. Y.P. Varshni, "Temperature Dependence of Energy Gap in Semiconductors," *Physica*, **34** [1] 149-154 (1967).
66. S.R. Dhariwal and V.N. Ojha, "Band-Gap Narrowing in Heavily Doped Silicon," *Solid-State Electron.*, **25** [9] 909-911 (1982).
67. R.A. Abram, G.N. Childs, and P.A. Saunderson, "Band-Gap Narrowing Due to Many-Body Effects in Silicon and Gallium-Arsenide," *J. Phys. C: Solid State Phys.*, **17** [34] 6105-6125 (1984).
68. V. Palankovski, G. Kaiblunger-Grujin, and S. Selberherr, "Study of Dopant-dependent Band Gap Narrowing in Compound Semiconductor Devices," *Mater. Sci. Eng., B*, **66** [1-3] 46-49 (1999).
69. W. Zagódzonwosik and W. Kuzmicz, "Physical-Mechanisms of Bandgap-Narrowing in Silicon," *Electron. Lett.*, **19** [14] 515-516 (1983).
70. R.J. Vanoverstraeten and R.P. Mertens, "Heavy Doping Effects in Silicon," *Solid-State Electron.*, **30** [11] 1077-1087 (1987).
71. R.T. Johnson, "Cadmium Sulfide Neutron Detectors - Annealing of Radiation Damage," *IEEE Trans. Nucl. Sci.*, **Ns17** [4] 14-19 (1970).
72. W. Qiu, H.X. Xu, N.J. Podraza, S.R. Phillipot, J.E. Baciak, S. Trolier-McKinstry, and J.C. Nino, "Analysis of the Band Structure of  $\text{BiI}_3$  Single Crystals via Optical and Computational Methods," *In Preparation*.
73. I.M. Dharmadasa, "Recent Developments and Progress on Electrical Contacts to CdTe, CdS and ZnSe with Special Reference to Barrier Contacts to CdTe," *Prog. Cryst. Growth Charact. Mater.*, **36** [4] 249-290 (1998).
74. C. Marinelli, L. Sorba, B.H. Muller, D. Kumar, D. Orani, S. Rubini, A. Franciosi, S. De Franceschi, M. Lazzarino, and F. Beltram, "Ohmic versus Rectifying Contacts through Interfacial Dipoles: Al/ $\text{In}_x\text{Ga}_{1-x}\text{As}$ ," *J. Cryst. Growth*, **202** 769-772 (1999).
75. J.F. Moulder, W.F. Stickle, P.E. Sobol, and K.D. Bomben, "Handbook of X-ray Photoelectron Spectroscopy", ULVAC-PHI, Inc., Chanhassen, 1995.

76. S. Leroy, F. Blanchard, R. Dedryvere, H. Martinez, B. Carre, D. Lemordant, and D. Gonbeau, "Surface film formation on a graphite electrode in Li-ion batteries: AFM and XPS study," *Surf. Interface Anal.*, **37** [10] 773-781 (2005).
77. Y. Takasu, K. Yasuda, Y. Matsuda, and I. Toyoshima, "Adsorption of CO on Gold and Gold-Modified Platinum," *Chem. Phys. Lett.*, **152** [1] 105-108 (1988).
78. J. Nakamura, I. Toyoshima, and K. Tanaka, "Formation of Carbidic and Graphitic Carbon from CO on Polycrystalline Cobalt," *Surf. Sci.*, **201** [1-2] 185-194 (1988).
79. M.C. Wu, S.Z. Dong, and A.R. Zhu, "Studies of CO Dissociation Promoted by Na on Ag(110)," *Surf. Sci.*, **216** [3] 420-428 (1989).
80. F.M. Ismail and Z.M. Hanafi, "Some Physicochemical Properties of Bismuth Chalcogenides X-Ray Photoelectron and Diffuse Reflectance Spectra," *Z Phys Chem-Leipzig*, **267** [4] 667-672 (1986).
81. Y. Schuhl, H. Baussart, R. Delobel, M. Lebras, J.M. Leroy, L. Gengembre, and J. Grimalt, "Study of Mixed-Oxide Catalysts Containing Bismuth, Vanadium and Antimony - Preparation, Phase-Composition, Spectroscopic Characterization and Catalytic-Oxidation of Propene," *J Chem Soc Farad T 1*, **79** 2055 (1983).
82. M. Schieber, T.E. Schlesinger, and R.B. James, "Semiconductors for Room Temperature Nuclear Detector Applications," *43* 561 (1995).
83. X.H. Zhu, Z.R. Wei, Y.R. Jin, and A.P. Xiang, "Growth and Characterization of a PbI<sub>2</sub> Single Crystal Used for Gamma Ray Detectors," *Cryst. Res. Technol.*, **42** [5] 456-459 (2007).
84. J.F. Condeles, R.A. Ando, and M. Mulato, "Optical and Structural Properties of PbI<sub>2</sub> Thin Films," *J. Mater. Sci.*, **43** [2] 525-529 (2008).
85. G.X. Zhang, D.Q. Yang, and E. Sacher, "X-ray Photoelectron Spectroscopic Analysis of Pt Nanoparticles on Highly Oriented Pyrolytic Graphite, Using Symmetric Component Line Shapes," *J. Phys. Chem. C*, **111** [2] 565-570 (2007).
86. L. Xiao and L.C. Wang, "Structures of Platinum Clusters: Planar or Spherical?," *J. Phys. Chem. A*, **108** [41] 8605-8614 (2004).

**DISTRIBUTION LIST**  
**DTRA-TR-12-70**

**DEPARTMENT OF DEFENSE**

DEFENSE TECHNICAL  
INFORMATION CENTER  
8725 JOHN J. KINGMAN ROAD,  
SUITE 0944  
FT. BELVOIR, VA 22060-6201  
ATTN: DTIC/OCA

**DEPARTMENT OF DEFENSE  
CONTRACTORS**

EXELIS, INC.  
1680 TEXAS STREET, SE  
KIRTLAND AFB, NM 87117-5669  
ATTN: DTRIAC